Front. Chem. China 2009, 4(3): 229–248
DOI 10.1007/s11458-009-0090-z

FEATURE ARTICLE

Chip calorimetry for fast cooling and thin films: a review

Wei CHEN[1,2], Dongshan ZHOU (✉)[1,2], Gi XUE[1] and Christoph SCHICK (✉)[2]

1 Department of Polymer Science and Engineering, State Key Laboratory of Co-ordination Chemistry, School of Chemistry and Chemical Engineering, Nanjing National Laboratory of Microstructures, Nanjing University, Nanjing, 210093, China
2 Institute of Physics, University of Rostock, Universitaetsplatz 3, 18051 Rostock, Germany

Here we review on the thin-film chip calorimeter with controllable cooling as well as heating rates up to $10^6\,K\cdot s^{-1}$ developed in the last 5 years at the Institute of Physics, Rostock University. The calorimeter has been successfully used for fast thermal processing and simultaneous calorimetric measurements of many polymer samples, the physical properties of which are generally dependent strongly on their thermal history. Besides, owing to the very small addenda heat capacity, the calorimeter is very sensitive to study samples of only several tenths of nanograms. With differential alternating current (AC) design, the sensitivity of the calorimeter increased to a few tenths of pico-Joules per Kelvin. Therefore, it can be used to study glass transition of polymers confined in ultra-thin films down to several nanometers thickness. After the discussion of the strategy to realize fast cooling, we describe the static and dynamic thermal properties of the sensors used for the setup of the calorimeter. Finally, we present examples to show the performance of the calorimeter in different measurement modes.

Keywords chip calorimeter, fast cooling, fast heating, metastability

1 Introduction

Fast cooling is commonly used to produce partially crystallized or totally amorphous polymers, metal alloys, and other materials for industrial applications and fundamental research [1–5]. A calorimeter that measures physical properties (e.g., heat capacity and enthalpy) of materials simultaneously during the fast thermal processing is very attractive. With the introduction of silicon nitride membrane technology, the performance of calorimeters has been greatly enhanced [6–10]. The heating–cooling rate, as well as the sensitivity of the thin-film calorimeter constructed on a submicron Si_3N_x membrane microchip module, can be pretty high mainly due to the very small addenda produced by the cell itself. Allen and coworkers [7,10] were the first to develop the thin-film differential scanning calorimeter (TDSC) using silicon nitride membranes for ultrafast heating. The cell of their calorimeter consists of a thin-film heater, Ni or Pt ~50 nm, deposited on a thin, ~30 nm Si_3N_x membrane. The heater simultaneously serves as a resistive thermometer. When operated under high vacuum conditions (~10^{-5}–10^{-6} Pa), the heating rates can reach as high as $10^7\,K\cdot s^{-1}$ and the sensitivity is approximately several tenths of pico-Joules per Kelvin [11–13]. This type of ultrafast quasi-adiabatic membrane calorimeters has been successfully used for heat capacity measurement of nanoparticles [6,8,14], ultrathin polymer films [9,15,16], and nanoparticles embedded in nanofilms [17,18].

While ultrafast heating can be realized by increasing the heating power and decreasing the heat capacity of the sample and addenda during a quasi-adiabatic heating process, the ultrafast cooling can only be achieved under nonadiabatic conditions with low total thermal inertia (sample, addenda, and heat transfer media) because the cooling rate of any system is restricted by the finite heat transfer from the system.

In recent years, starting from a commercially available thin-film vacuum sensor (thermal conductivity vacuum gauge, TCG-3880, Xensor Integration, NL) [19] fabricated on submicron silicon nitride film, we built a chip calorimeter with controllable cooling as well as heating rates up to $10^4\,K\cdot s^{-1}$ in polymer and polymer nanocomposites [20]. The method was successfully applied to study melting, crystallization, and recrystallization of poly(ethylene terephthalate) (PET) [21,22], polyethylene (PE) [20,23–25], polypropylene (PP) [26–28], poly(butylene terephthalate) (PBT) [29],

Received March 19, 2009; accepted March 23, 2009
E-mail: dzhou@nju.edu.cn, christoph.schick@uni-rostock.de

polyamide blends [30], and isotactic polystyrene (iPS) [31]. With a series of newly designed sensors, we are now able to process samples and perform measurements with scanning rates up to $10^6\,K\cdot s^{-1}$ [32]. Isothermal calorimeter [33] and differential AC calorimeter [34–37] are also built based on the fast scanning chip calorimeters. The isothermal calorimeter has a time resolution in milliseconds, hence can be used to study the isothermal crystallization kinetics of fast crystallizing polymers, such as PAL, isotactic polypropylene (iPP), and PE. Differential AC calorimeter was used for the study of glass transition of polymers confined in ultrathin films of about several nanometers thick because it has a very high sensitivity (~$50\,pJ\cdot K^{-1}$) and a wide modulation frequency range (10^{-1}–10^3 Hz).

We focus our review on the non-adiabatic chip (thin-film) calorimeter with fast cooling as well as heating rates built in this laboratory. The main text is organized into three sections. In Section 2, the strategy to realize the fast cooling is analyzed in detail. In Section 3, we describe the static and dynamic thermal temperature properties of sensors for the setup of fast scanning calorimeter. In Section 4, we present examples to show the performance of the calorimeters in different measurement modes.

2 How to make cooling fast?

To realize calorimetry at high scanning rates, addenda and sample should have sufficiently small heat capacity. The cooling agent must be thermally "inertia less" as well, which means it must have a small heat capacity as shown below. There are two possibilities to produce a fast cooling device: (i) using a solid heat sink (cold finger, as shown in Figure 1) made from high thermal conducting materials, such as metals, but adding a large heat capacity to the system; (ii) using low thermal conducting gas with very low heat capacity as the cooling medium. In order to make a decision which method is best suited for fast cooling, we estimate the maximum cooling rate for both cases.

2.1 Upper limit of fast cooling with "heat sink"

First, we determine the upper limit of the scanning rate for a "cold finger" system as shown in Figure 1.

A cell with sample is placed at the flat face of a uniform rod with a specific heat capacity c, density ρ, thermal conductivity λ, and length L. The other face of the rod is coupled with a massive cooler, which is kept at a low temperature T_0. The temperature of the sample/rod interface is controlled by a thin flat heater with negligible heat capacity and thermal resistance. Ideal thermal contacts are assumed between the sample and the heater as well as between the heater and the rod. To determine the upper limit of the scanning rate, first we suppose the heat capacities of the cell and the sample are small enough to be neglected. A uniform heat flux $q(t)$ is supplied to the face of the rod at $z = 0$ and transmitted along the rod axis. The heat leakage from the lateral surface of the rod is negligible. The temperature distribution in the rod $T(z,t)$ is described by Fourier's heat transfer equation:

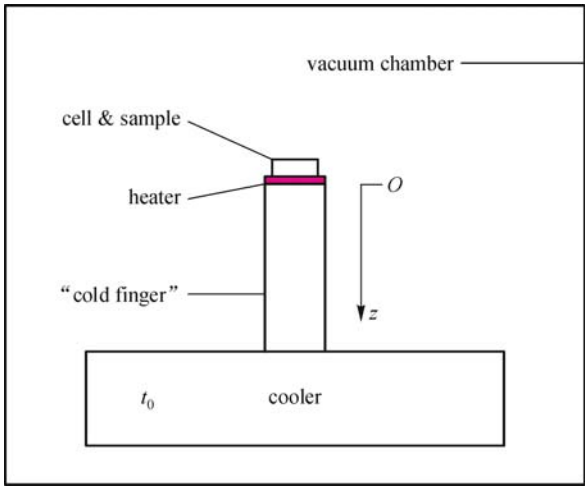

Figure 1 Scheme of the system with a "cold finger". The cell with the sample is placed at the flat face of a "cold finger" that is coupled with a cooler at a low temperature T_0. The temperature of the sample is controlled by a thin heater located at the face of the finger.

$$\rho c\cdot\partial T(z,t)/\partial t = \lambda\cdot\partial^2 T(z,t)/\partial z^2. \quad (1)$$

Usually, the sample temperature is scanned linearly with time. Consider a sawtooth-shaped heating–cooling process with a period τ_0 and amplitude T. The sample temperature is driven by a periodic heat flux $q(t)$ with an amplitude q_0 (the flux is changed in the range from 0 to $2q_0$). This periodic process can be presented as a sum of harmonic functions with periods $\tau_0/(2n+1)$ at $n = 0, 1, 2, \ldots$. According to Eq. (1), the amplitude T_{A0} of the temperature oscillation of the rod surface $z = 0$ at the frequency $\omega_0 = 2\pi/\tau_0$ equals to $q_{A0}/(\omega\rho c\lambda)^{1/2}$, provided the thermal length $l_0 = (2\lambda/\omega_0\rho c)^{1/2}$ is small with respect to L, where $q_{A0} \sim q_0$ is the heat flux amplitude at ω_0. The temperature of the rod surface is oscillating around the average value $T_{AV} = T_0 + T_B$, where the bias temperature T_B equals to $\sim q_0 L/\lambda$. The amplitude of the temperature oscillations can be enhanced by varying the parameters in the relation $T_{A0} = q_{A0}/(\omega_0\rho c\lambda)^{1/2}$, but T_{A0} cannot be larger than T_B.

Generally, the parameter $c\rho$ of condensed materials does not depend essentially on the chosen material (except for the low temperature region that is not considered at this

point). For example, for metals, $c\rho$ ranges from a minimum of $1.9 \times 10^5\ J\cdot K^{-1}\cdot m^{-3}$ (lithium) to a maximum of $2.5 \times 10^7\ J\cdot K^{-1}\cdot m^{-3}$ (silver) and over 75% of them equal to $(2\pm1) \times 10^6\ J\cdot K^{-1}\cdot m^{-3}$ at room temperature. To increase the amplitude T_{A0} at a fixed q_{A0}, one can choose a material with small thermal conductivity; but the choice is limited by the following restriction $\lambda_{min} = q_0 L/T_{B,max}$, where $T_{B,max}$ is the maximal allowed bias temperature. For example, the minimal appropriate thermal conductivity λ equals to $25\ W\cdot K^{-1}\cdot m^{-1}$ with the following predetermined parameters: $q_0 = 2 \times 10^5\ W\cdot m^{-2}$ ($20\ W\cdot cm^{-2}$), $L = 0.05$ m, and $T_{B,max} = 400$ K.

Next, the scanning rate can be estimated as the rate at the main harmonic: $\omega_0\cdot T_{A0} \sim q_0(\omega_0 / \rho c\lambda)^{1/2}$. The rate increases with the increasing of angular frequency ω_0 (or the decreasing of period τ_0). On the other hand, the scanning period τ_0 should satisfy the relationship $dT/dt\cdot \tau_0 \sim q_0/(\omega_0\rho c\lambda)^{1/2} \sim \Delta T$, where ΔT is the scanning range as required by the scanning experiment. Therefore, $\tau_0 \sim 2\pi\rho c\lambda(\Delta T)^2/q_0^2$. Finally, the scanning rate dT/dt can be estimated as the ratio of the peak-to-peak amplitude $2\Delta T$ and the time interval $\tau_0/2$: $dT/dt \sim q_0^2/(2\pi\rho c\lambda\cdot\Delta T)$. Given the minimal λ, one gets the maximal scanning rate:

$$(dT/dt)_{max} \sim [q_0/(\rho cL)]\cdot(T_{B,max}\ /\Delta T) \qquad (2)$$

or

$$(dT/dt)_{max} \sim [q_0^2/(\rho c\lambda)]\cdot(1/\Delta T). \qquad (3)$$

Now we can estimate the upper limit of $(dT/dt)_{max}$ of the metal "cold finger" strategy with the following realistic parameters: $q_0 = 2 \times 10^5\ W\cdot m^{-2}$, $\Delta T = 100$ K, $T_{B,max} = 400$ K, and $L = 0.05$ m. For all metals, their $c\rho\lambda$s change from $9.26 \times 10^6\ W^2\cdot s\cdot m^{-4}\cdot K^{-2}$ (bismuth) to $1.06 \times 10^{10}\ W^2\cdot s\cdot m^{-4}\cdot K^{-2}$ (silver), so that the upper limit of $(dT/dt)_{max}$ for the metal "cold finger" strategy is below $10^2\ K\cdot s^{-1}$. The scanning rate can be further increased by decreasing the temperature scanning range $2\Delta T$. However, this is not desired for a scanning calorimeter setup. Actually, for any scanning range ΔT in the range $\Delta T \leqslant T_B \leqslant T_{B,max}$ or equivalently τ_0 in the range of $\tau_0 \leqslant \tau_0\cdot T_B^2/(\Delta T)^2 \leqslant \tau_0\cdot T_{B,max}^2/(\Delta T)^2 = \pi c\rho L^2/\lambda_{min}$, the product of scanning rate and the scanning range $(dT/dt)\cdot\Delta T$ is invariant with respect to the range ΔT or period τ_0. This results from the fact that $dT/dt \sim \tau_0^{-1/2}$ while $\Delta T \sim \tau_0^{1/2}$.

Actually, Eq. (3) indicates that the upper limit of $(dT/dt)_{max}$ can be greatly increased if gases are used as heat transfer agents owing to their very small value products of $c\rho$ and λ. For example, $c\rho\lambda$ of N_2 at 10^5 and 10^3 Pa is $3.2 \times 10^1\ W^2\cdot s\cdot m^{-4}\cdot K^{-2}$ and $3.2 \times 10^{-1}\ W^2\cdot s\cdot m^{-4}\cdot K^{-2}$, respectively. Therefore, $(dT/dt)_{max}$ would be as large as $\sim 10^7\ K\cdot s^{-1}$ and $10^9\ K\cdot s^{-1}$, respectively. Of somehow anti-intuitive is that λ should also be as small as possible to increase $(dT/dt)_{max}$. This is true for the metal "cold finger" strategy but wrong for the nonadiabatic thin-film (chip) calorimeter that will be discussed below. Otherwise, we will get the misleading result that adiabatic chip calorimeter in the vacuum is the best way to realize the ultrafast cooling owing to the infinitesimal value of $c\rho\lambda$.

2.2 Nonadiabatic thin-film scanning calorimetry with gas cooling agent

According to Eq. (3), a kind of gas is the best cooling agent for the fast scanning calorimetry. Also the addenda and the sample heat capacity should be as small as possible. Therefore, thin-film calorimetry is ideal for fast scanning experiments. We will consider the limitations of the scanning rate in the following two geometries. The first is a plate-like sample and the second is a point-like sample placed at a thin-film membrane, which serves as a heater and a support. In both cases, the film heater is very thin and the heat transfer along the membrane is negligible. In the first case, a thin-film sample of thickness d_s is deposited on the membrane. The film system is placed in a kind of gas with the following parameters: ρ_g, c_g, and λ_g. The corresponding parameters of the sample are ρ_s, c_s, and λ_s. The distance between the film and the thermostat wall L is small with respect to the film lateral dimensions a and b. The temperature of the thermostat T_0 is kept constant. To estimate the upper limit of the cooling rate, we assume that the distance L is small with respect to the thermal length in the gas $l_g = [\lambda_g\tau_0/(\pi\rho_g c_g)]^{1/2}$, which in the case of nitrogen gas at pressures in the range of 10^3 to 10^5 Pa equals to ~0.8 to 8 mm at $\tau_0 = 0.1$ s ($\rho_g = 1.2\ kg\cdot m^{-3}$, $c_g = 1.04 \times 10^3\ J\cdot kg^{-1}\cdot K^{-1}$, and $\lambda_g = 0.026\ W\cdot K^{-1}\cdot m^{-1}$ at room temperature and normal pressure). Then the heat flow from the sample into the wall equals to $\Phi = \lambda_g ab(T - T_0)/L$, where T is the sample temperature (we neglect the heat transfer in other directions). Note that at increasing distance L the heat flow becomes smaller. In the case when $L > l_g$, the heat flow tends to be $\lambda_g ab(T - T_0)/l_g = ab(T - T_0)\ [\pi\tau_0^{-1}(\rho_g c_g\lambda_g)]^{1/2}$.

The maximal cooling rate can be estimated from the relation $(C_s + C_A)\cdot dT/dt = \lambda_g ab(T - T_0)/L$, where the total heat capacity of the sample $C_s = abd_s\rho_s c_s$. Assume that the addenda heat capacity C_A can be neglected, the maximal possible rate $(dT/dt)_{max} = \lambda_g(T - T_0)/(Ld_s\rho_s c_s)$. Thus, $(dT/dt)_{max}$ is $\sim 7 \times 10^3\ K\cdot s^{-1}$ at $L = 100$ μm, $T - T_0 = 500$ K, $d_s = 10$ μm, $\rho_s c_s = 2.0\times 10^6\ J\cdot K^{-1}\cdot m^{-3}$, and $\lambda_g = 0.026\ W\cdot K^{-1}\cdot m^{-1}$.

In the second case, consider a small disk-shaped sample of a thickness d_s and a radius r_0 placed on a thin-film heater of the same radius located at the membrane center. The distance from the heated region to the thermostat wall L and the thermal length in the gas l_g are large with respect to the radius

r_0. Here, we assume that the radius r_h of the heated region equals r_0. However, as will be shown in the next section, r_h will change with the scanning rate. But at high enough scanning rates, $r_h \approx r_0$ can be justified. Then, at any relation between L and l_g, the heat flow Φ from the point-like source of radius r_0 to the gas can be estimated as $\Phi = -4\pi r^2 \lambda_g dT_g(r)/dr$ at $r = r_0$, where the temperature in the gas around the heater equals to $T_g(r) = T_0 + (T - T_0)r_0/r$. Consequently, the heat flow from the sample into the gas equals to:

$$\Phi = (T - T_0) \cdot G, \tag{4}$$

where $G = 4\pi r_0 \lambda_g$ is the heat exchange parameter measured in $W \cdot K^{-1}$; it depends on the gas thermal conductivity and the size of the heated region. For r_0 = 40 μm, the parameter G equals to $\sim 10^{-5}$ $W \cdot K^{-1}$ in N_2 atmosphere at pressures in the range 10^3 to 10^5 Pa and room temperature [20–22]. It can be several times larger in helium gas. The estimated G based on Eq. (4) is in agreement with the measured value.

Then the maximal cooling rate in air can be estimated as $(dT/dt)_{max} \approx 4\lambda_g(T - T_0)/(r_0 d_s \rho_s c_s)$, when the addenda heat capacity C_A is negligible. Thus, at $T - T_0$ = 300 K, d_s = 5 μm, and $\rho_s c_s = 2.0 \times 10^6$ $J \cdot K^{-1} \cdot m^{-3}$, $(dT/dt)_{max}$ equals to $\sim 10^5$ $K \cdot s^{-1}$ in the nitrogen gas and $\sim 5 \times 10^5$ $K \cdot s^{-1}$ in the helium gas.

The second case is very promising. The rate $(dT/dt)_{max}$ can be even faster at smaller sample and heater dimensions as long as the radius is large enough and the membrane thickness d_0 and d_s is small enough to neglect the thermal gradient in the sample. The shapes of the heated region and the sample do not have effect on the heat transfer into the gas if the thermal length l_g is large with respect to r_0.

The limitation of the scanning rate arising from the thermal gradient in the sample can be estimated as following: if the maximal acceptable temperature difference across the sample equals to δT_s, then the limiting rate is $(dT/dt)_{max} = \delta T_s \lambda_s / (\rho_s c_s d_s^2)$. Therefore, the maximal thickness d_s should not exceed 1 μm for $\rho_s c_s = 2 \times 10^6$ $J \cdot K^{-1} \cdot m^{-3}$, λ_s = 0.3 $W \cdot K^{-1} \cdot m^{-1}$, $(dT/dt)_{max}$ equals to $\sim 10^6$ $K \cdot s^{-1}$, and δT_s = 3 K.

Another limitation of the heating rate generates from the thermal contact between the sample and the heater. The temperature difference δT_c at the thermal contact between the sample and the heater should not be too large; that is, the thermal contact resistance must be sufficiently small. The maximal heat flux from the heater to the sample equals to $\sim \rho_s c_s d_s (dT/dt)_{max}$. On the other hand, the heat flux through the contact is $q_c = R_c^{-1} \delta T_c$ by definition of the thermal contact conductance R_c^{-1} measured in $W \cdot m^{-2} \cdot K^{-1}$. Therefore, we can estimate $(dT/dt)_{max} \sim \delta T_c / \rho_s c_s d_s R_c$. Generally, the contact conductance measured between a dry joint of polished surfaces equals to $\sim 2 \times 10^3$ $W \cdot m^{-2} \cdot K^{-1}$ and increases with contact pressure and temperature [38–40]. The thermal contact conductance becomes 10^2 times larger if adhesive grease is used to improve the contact. Generally, the conductance R_c^{-1} can be 10^5 to 10^6 $W \cdot m^{-2} \cdot K^{-1}$ for contacts with adhesive materials [41]. The adhesion between a polymer and the membrane becomes nice after first melting. Suppose the thermal contact conductance for the polymer/membrane interface is of the order of 5×10^5 $W \cdot m^{-2} \cdot K^{-1}$. Then the limit of the scanning rate is $\sim 1.2 \times 10^6$ $K \cdot s^{-1}$ for δT_c = 5 K, $\rho_s c_s = 2 \times 10^6$ $J \cdot K^{-1} \cdot m^{-3}$, and d_s = 1 μm. However, when melting, the apparent heat capacity can be of the order of 10^7 $J \cdot K^{-1} \cdot m^{-3}$ (10 $J \cdot g^{-1} \cdot K^{-1}$) [20,21]. In this case, the rate limit equals to $\sim 2.5 \times 10^5$ $K \cdot s^{-1}$. The effect of the thermal contact resistance can be reduced with the decreasing of sample thickness.

In conclusion, the strategy to realize ultrafast cooling is to use a tiny sample placing on a point-like heater of several tenths of microns and running in the low thermal inertia gas atmosphere. In this case, the cooling and heating rate can be estimated by the equation $(dT/dt)_{max} \approx 4\lambda_g(T - T_0)/(r_0 d_s \rho_s c_s)$ if the addenda heat capacity is neglectable. Therefore, controllable cooling and heating rates up to 10^6 $K \cdot s^{-1}$ can be achieved if the diameter of the sample is within ~20 μm and the thickness is within ~1 μm.

3 Static and dynamic thermal properties of sensors for the calorimeter

Nonadiabatic thin-film (chip) calorimeter for ultrafast thermal processing and simultaneous measurements with submillisecond resolution and $pJ \cdot K^{-1}$ sensitivity can be constructed using silicon nitride membrane technology. Commercially available gauges from Xensor Integration, NL, can be utilized for this purpose.

The first sensor available was the thermal conductivity gauge TCG-3880 as shown in Figure 2. It consists of a submicron (~0.5 μm) amorphous silicon nitride membrane with a thin-film thermopile and a resistive film heater located at the center of the membrane. The heater strips and all electrical leaders (including thermopile) are formed by *p*- and *n*-type polysilicon tracks with specified thermoelectric properties and resistivities. The size of two parallel heater strips are ~5 μm × 100 μm and they are separated by ~20 μm. All electrical connections are covered by additional 0.7 μm SiO_2 layer for electrical insulation and protection. The six thermopile hot junctions and the white spots around the central region in the photograph are arranged around the central heated area of ~50 μm × 100 μm. The cold junctions are placed at the silicon frame fixing the membrane at a distance of ~1 mm from the center. Thus the cold junction

temperature equals to the temperature of the holder, which is close to the temperature of the thermostat. An additional copper–constantan thermocouple was utilized for the measurement of the holder temperature, which was used as the reference temperature T_0.

The silicone frame with the membrane is bonded to a standard chip carrier as shown in Figure 2. The whole assembly can be taken out of the thermostat and positioned under a microscope for sample handling. The gauge being installed in a thermostat with controlled temperature; gas pressure can be utilized as a sensor for the fast scanning calorimetry of submicrogram samples.

The TCG-3880 is not optimized for calorimetry since the thermometer (thermopile junctions) is placed ~50 μm away from the heated region. This separation results in the measured temperature being shifted and delayed from the temperature of the heater/sample interface. The temperature calibration is a non-trivial task even with the knowledge of the temperature distribution in the membrane. Therefore, in the new sensors, the thermopile hot junctions are arranged in the central part of the heated area between the heater stripes. A set of sensors with different dimensions of heated area is now available. For example, the sensor XEN-3969 has the size of the central heated part of 14 μm ×14 μm and can be used for scanning rates over $10^6\,\mathrm{K\cdot s^{-1}}$; while sensor XEN-2972 has a largest size of smooth heated area of 100 μm × 100 μm and is suitable for the measurement of ultrathin films.

Although a point-like heating source is assumed, it is very important to know the dynamic thermal properties of the sensors, for example, the addenda heat capacity, the temperature distribution in the membrane and the ambient gas. This is required for a better understanding of the thin-film calorimeter and for the development of even better sensors.

3.1 Temperature distribution in the membrane and addenda heat capacity

We will consider a volume element dxdydz around the heater in the membrane plane in the Cartesian coordinate system, as shown in Figure 3, with the origin O at the center of the membrane, axis Oz perpendicular to the membrane, and axes Ox and Oy are correspondingly parallel and perpendicular to the heater strips. A flat wall (the holder) is assumed to be located parallel to the membrane at $z = L$ and the temperature of the wall equal to the thermostat temperature T_0. Because the membrane thickness $d_\mathrm{m} \approx 0.5$ μm is assumed to be negligibly small, we then need to consider the two-dimensional temperature distribution $T(x,y)$ within the membrane plane. During steady-state heating, the heat flow along the membrane into a volume element dxdyd$_\mathrm{m}$ equals to $\lambda_\mathrm{m}(\partial^2 T/\partial x^2 + \partial^2 T/\partial y^2)dxdyd_\mathrm{m}$ and it is balanced by the heat flow $q_\mathrm{g}(x,y)$dxdy into the gas from the surface increment dxdy. The temperature distribution in the gas and the heat flux $q_\mathrm{g}(x,y)$ can be calculated analytically when the membrane temperature $T(x,y)$ is determined [42].

The function $T(x,y)$ can be estimated by assuming that the heat transfer through the gas is proportional to the temperature difference $T(x,y) - T_0$. Then the heat flow from the surface increment dxdy into the gas approximately equals to λ_gdxd$y(T - T_0)/L$. This assumption is in good agreement with experiments. Therefore we have a heat balance equation with separable variables:

$$\partial^2 T/\partial x^2 + \partial^2 T/\partial y^2 = k^2(T - T_0), \tag{5}$$

where $k^2 = \lambda_\mathrm{g}/\lambda_\mathrm{m} d_\mathrm{m} L$, $T = T_0 + X(x)Y(y)$, and $(1/X)\partial^2 X/\partial x^2 + (1/Y)\partial^2 Y/\partial y^2 = k^2$.

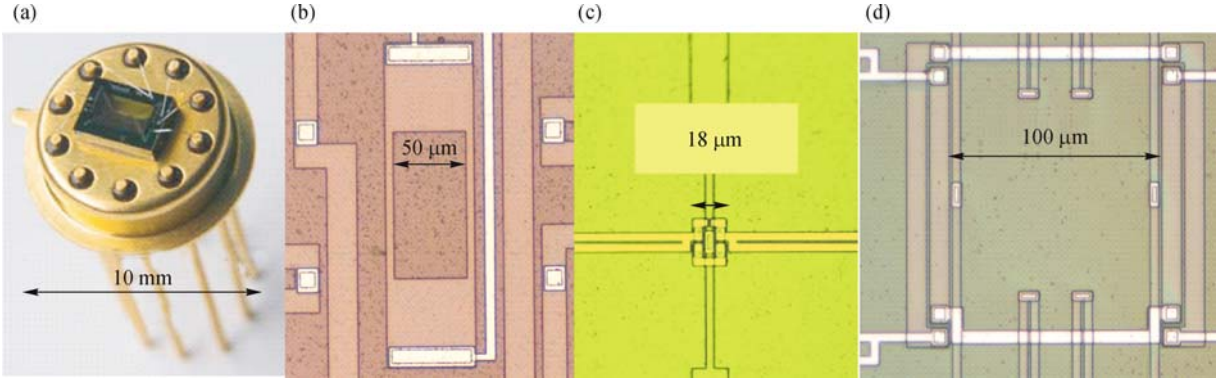

Figure 2 (a) chip sensor TCG-3880 (Xensor Integration, NL) mounted onto a standard chip carrier; (b) magnified center area of the membrane of sensor TCG-3880 with the heater indicated by the arrow and four hot junctions of the thermopile by bright squares; (c) magnified center area of the membrane of XEN-3973 with very small heated area; and (d) one thermal couple between the heater. The sensor can be used for the control of heating and cooling with rates over $10^6\,\mathrm{K\cdot s^{-1}}$, magnified center area of the membrane of XEN-2972 with very relative large heated area, and six thermal couples between the heater. It can be used for the measurement of ultrathin film in the differential AC mode with best sensitivity of ~50 $\mathrm{pJ\cdot K^{-1}}$.

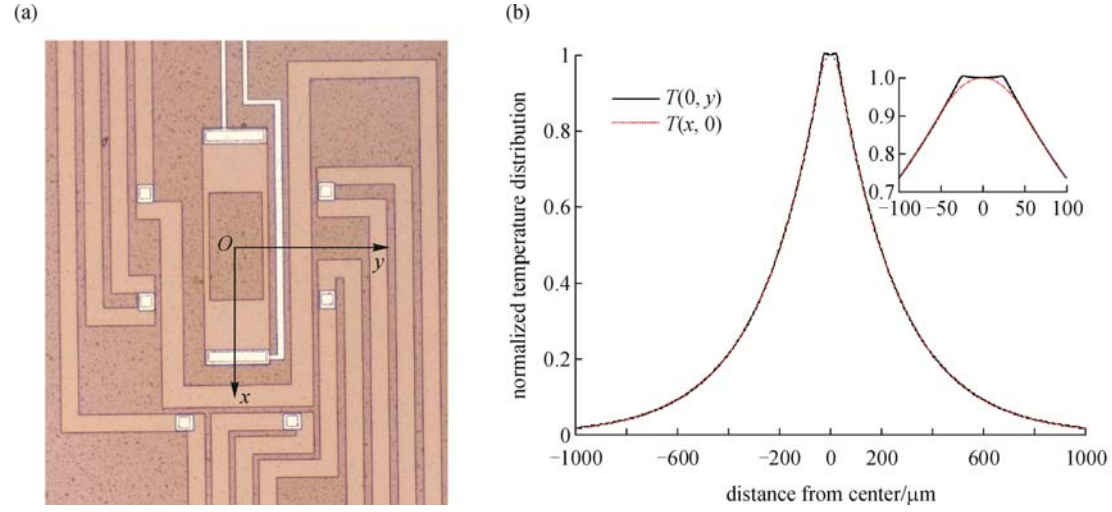

Figure 3 (a) Cartesian coordinate system used for the determination of the temperature distribution $T(x, y)$ in the membrane plane and the gas atmosphere; (b) normalized temperature distribution $T(0, y)$ and $T(x, 0)$ in the membrane.

Thus, for a point-like heat source located at the origin O, the temperature distribution equals to:

$$T(x,y) = T_0 + (T^* - T_0)\exp(-\xi|x|)\exp(-\xi|y|), \quad (6)$$

where T^* is the temperature at the origin O and ξ^{-1} equals to $(2Ld_m\lambda_m/\lambda_g)^{1/2}$ in the case of an isotropic membrane. Eq. (6) is valid when the length ξ^{-1} is small with respect to the distance from the heated area to the membrane periphery, that is, the temperature drops significantly at the membrane periphery. Hence, the boundary conditions at the membrane periphery do not essentially affect the shape of the temperature distribution near the heater. This is the case in the sensor design because ξ^{-1} is ~250 μm at $d_m \approx 0.5$ μm, $L \approx 0.5$ mm, $\lambda_g \approx 0.026\ W\cdot K^{-1}\cdot m^{-1}$, and $\lambda_m \approx 3\ W\cdot K^{-1}\cdot m^{-1}$ [43].

Actually, the heater consists of two stripes oriented along the Ox axis and located at $y = \pm y_0$. The length and separation of the heater strip change with different sensors. For TCG-3880, y_0 equals to ~25 μm, length b is ~100 μm, and the width of the heater a is ~ 5 μm. Therefore, by integrating along the stripe surface, we obtain the final temperature distribution in the membrane:

$$T(x,y) = T_0 + (T^* - T_0)X_0^{-1}Y_0^{-1}\int_{-b/2}^{b/2} X(x,\beta)\mathrm{d}\beta \int_{-a/2}^{a/2} Y(y,\alpha)\mathrm{d}\alpha, \quad (7)$$

where $X(x,\beta) = \exp(-\xi^{-1}|x-\beta|/\mu), Y(y,\alpha) = \exp(-\xi^{-1}\cdot|y-y_0-\alpha|) + \exp(-\xi^{-1}|y+y_0+\alpha|)$ and the normalizing constants $X_0^{-1} = \int_{-b/2}^{b/2} X(0,\beta)\mathrm{d}\beta$, $Y_0^{-1} = \int_{-a/2}^{a/2} Y(0,\alpha)\mathrm{d}\alpha$.

The dependence of $T(x,y)$ determined by Eq. (7) is shown in Figure 3(b). The temperature difference $T(x,0) - T_0$ at 1 mm from the membrane center is below 2% of $T^* - T_0$. Thus the assumption that the boundary condition at the membrane periphery is not essential to the shape of the temperature distribution $T(x,y)$ is correct. The function $T(x,y)^4$ is in good agreement with the measured fast infrared thermographic intensity $I(x,y)$ for DC heating at different powers and with quasi-static oscillating heating–cooling conditions [44].

When deviated from quasi-static conditions, the dynamic heat transfer problem for the membrane placed in a gas is described by the following equation, obtained in the same way as for the quasi-static conditions:

$$\partial^2 T/\partial x^2 + \partial^2 T/\partial y^2 = k^2(T - T_0) + (1/D_m)\partial T/\partial t, \quad (8)$$

where $D_m = \lambda_m/(\rho_m c_m)$ is the thermal diffusivity of the membrane.

In the case of stationary harmonic temperature oscillations excited by a point source located in the membrane center, the solution of Eq. (8) equals to $T(x,y,t) = T_t + T_\omega \exp[i(\omega t - k_x x - k_y y)] \exp(-\xi_x x - \xi_y y)$. The temperature oscillations exponentially decay with the distance from the source at characteristic length $1/\xi$ described by:

$$(\xi + ik)^2 = \xi_0^2 + i\omega/D_0, \quad (9)$$

where $\xi^2 = \xi_x^2 + \xi_y^2$, $k^2 = k_x^2 + k_y^2$. This is the dispersion law of the thermal waves in the membrane. The complex

Eq. (9) is equivalent to the relations $k = \omega/(2\xi D_0)$ and $\xi^2 = \xi_0^2 + [\omega/(2\xi D_0)]^2$. From the last relation as follows:

$$\xi(\omega)^2 = \frac{1}{2}\xi_0^2\left(1 + \sqrt{1 + \left(\frac{\omega}{\omega_0}\right)^2}\right), \quad (10)$$

where $\omega_0 = \xi_0^2 D_0 = \lambda_g/(\rho_m c_m d_m L)$. ω_0 is the characteristic maximum frequency beyond which the quasi-static temperature distribution changes in the membrane.

We consider a sawtooth-shaped heating–cooling process with the period τ_p, the scanning temperature range ΔT, and the rate $R = 2\Delta T/\tau_p$. This periodic process can be expressed as a sum of harmonic oscillations. The characteristic length $1/\xi(R)$ for this scanning process is of the order of the length $1/\xi(\omega)$ for the main harmonic $\omega = 2\pi/\tau_p$ of the sawtooth process. Then, $\xi(R)$ is expressed as:

$$\xi(R)^2 = \frac{1}{2}\xi_0^2(1 + \sqrt{1 + (R/R_0)^2}), \quad (11)$$

where $R_0 = 2\Delta T\omega_0$; correspondingly, it is the characteristic maximum scanning rate beyond which the quasi-static temperature distribution changes in the membrane.

The effective radius of the heated region of the membrane can be estimated as a sum of $r_0 + \alpha/\xi(R)$, where α is a dimensionless parameter of the order of 1. Actually, we obtained from experiments that α equals to ~0.2 [24,32]. Then the addenda heat capacity can be estimated as $C_A \approx \pi\rho_m c_m d_m[r_0 + \alpha/\xi(\omega)]^2$. Substituted with Eq. (11), we get:

$$C_A(T,R) = C_0\left(1 + \frac{a}{\{1 + [1 + (R/R_0)2]^{1/2}\}^{1/2}}\right)^2, \quad (12)$$

where $C_0 = \pi r_0^2 d_m \rho_m c_m$ and $a = \sqrt{2}\alpha/(r_0\xi_0)$.

At low frequency or scanning rate, C_A equals to the static value $\pi(r_0 + \alpha/\xi_0)^2 d_m \rho_m c_m$; at high enough rate, C_A is determined only by the center heated area $\pi r_0^2 d_m \rho_m c_m$. The experimental dependence of C_A versus R for different sensors in different gas atmosphere has been studied. The measured dependence is found to be well described by Eq. (12) with realistic parameters.

3.2 Temperature distribution in a gas around the membrane

The heat transfer from the heated region to the environment through the nitrogen gas is much larger than through the membrane only because the membrane is very thin [20–22, 45]. The heat transfer from the heated area to the environment can be described by a heat exchange parameter G measured in $W \cdot K^{-1}$. It is shown from the pressure calibration curve of the TCG-3880 that at pressures below 0.1 Pa, the gauge output voltage is 10 times larger when only heat transfer through the membrane exists compared with the output voltage at atmospheric pressure when the heat transfer through the gas is dominant. As the gauge output voltage is proportional to the temperature difference ΔT between the heater and the environment and ΔT is inversely proportional to the heat exchange coefficient G, the heat transfer through the gas at atmospheric pressure is ~10 times larger than that through the membrane. The heat transfer through the gas can still be increased by several times, provided the helium gas is utilized instead of the nitrogen gas. The heat flow from the heated region due to radiation emission does not exceed 1% to 2% of the heat transfer through the gas at $T^* = 600$ K and $T_0 = 300$ K; also the convective heat transfer is insignificant for a small heated region of ~100 μm at reduced pressures as proved by Minakov [44]. Therefore the thermal conduction from the heated region through the gas is dominant.

The main features of the temperature distribution in the gas around the membrane have been studied analytically and numerically using a model with an analytical solution [44]. It is found that the linear approximation for the thermal gradient in the gas between the membrane and the wall is not perfect at least in the neighborhood of the membrane center. The gradient near the membrane center is larger than $(T - T_0)/L$. On the other hand, the linear approximation $(T - T_0)/L$ is correct outside the ~100 μm central region. As a result, the temperature distribution in the central part of the membrane is smeared with respect to the exponential distribution $T(x,y)$ obtained in the previous section, but this smearing is insignificant because the heater size also equals to ~100 μm. Thus, the actual temperature distribution is well described by Eq. (7) even in the middle of the membrane.

The heat flux in the lateral directions of the gas is found to be of the same order of magnitude as that along the z direction. The central heated region can be considered as a small (point-like) source of the heat flow into the gas because of the nearly spherical temperature distribution around the heated region. As proven in Section 2, in the point-like heating source approximation, the heat flow from the heated region into the environment equals to $G(T^* - T_0)$, where $G = 4\pi r_0 \lambda_g$ is the heat transfer coefficient through the gas. Thus, at room temperature in the nitrogen gas, the estimated value G equals to ~2×10^{-5} $W \cdot K^{-1}$. It can be several times larger the in helium gas. As a comparison, the heat flow from the heater perimeter P into the membrane equals to

$$G_m(T^* - T_0) \approx \lambda_m d_m P(T^* - T_0)\xi, \quad (13)$$

where the perimeter of the heater $P \approx 2\pi r_0$ and the heat transfer coefficient through the membrane $G_m \approx 2\xi\pi r_0 \lambda_m d_m$. Then, in the steady-state or in the quasi-static state, G_m equals to ~2×10^{-6} $W \cdot K^{-1}$ at $(1/\xi) \approx 250$ μm at $d_m \approx 0.5$ μm, and

$\lambda_m \approx 3\ W \cdot K^{-1} \cdot m^{-1}$, which is one order of magnitude smaller than G.

4 Experiments with chip calorimeter

In this section, we present examples to verify the performance of calorimeters based on the thin-film sensors. These are mostly on but not limited to the studies of polymer systems.

4.1 Scanning calorimeter

A sensor as described in the previous section was placed into a temperature-controlled oven (see Figure 4). A vacuum-shielded oven originally designed for an AC calorimeter [46] was used for all experiments. The internal volume can be filled with some gas at controlled pressure between 10 Pa and 100 kPa. The whole construction fits into a Dewar vessel with liquid nitrogen for cooling. A thin-wire copper–constantan thermocouple was located close to the sensor in order to measure surrounding gas temperature. The cold junction temperature of the sensor thermopile on the silicon frame was assumed to be equal to the measured gas temperature.

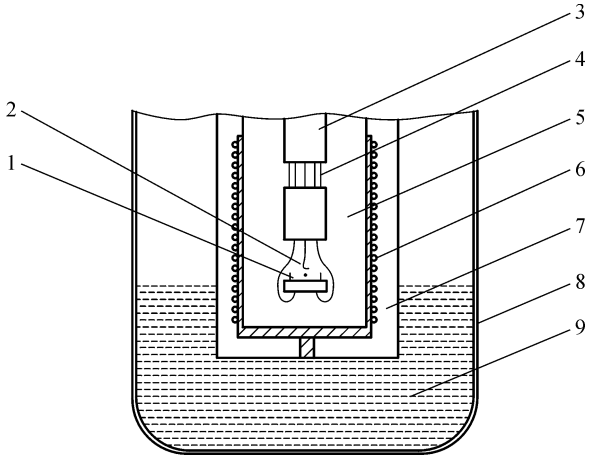

Figure 4 The oven of the calorimeter (not to scale). (1) sensor; (2) thermocouple to measure gas temperature; (3) thin wall tube; (4) connector; (5) internal volume (pressure controlled); (6) heater; (7) external volume (vacuum); (8) Dewar vessel and (9) liquid nitrogen.

For studies of fast melting and crystallization, the sample must be small enough and stay at the heater during thermal cycling so that the adhesion between the sample and the cell could be sufficiently good. A tiny grain of polymer sample, normally ~100 to 500 ng, was transferred to the membrane using a soft cooper wire (diameter of 50 μm) to prevent the damage to the sensor film (~0.5 μm). A stereomicroscope was used to control the movement. When the sample was on the right place, an electrical current through the heater was switched on to melt the sample for the first time. In this way the sample was fixed at a position just on top of the heater. Because of strong adhesive forces, the sample membrane thermal contact was good and very stable after a few heating–cooling cycles, which is important for calorimetric measurements [47,48]. For the study of metals or other materials (the thermal contact with the sensor is not as good), ~1 μm layer of Apiezon^{TM}-N grease [49] was utilized as lubricant for good thermal contact between the sample and the membrane.

The resistive film heater, ~600 Ω, provides the heat flow $P_0(t)$, which is supplied to the membrane/sample interface and propagates through the sample, the membrane, and the ambient gas. The equation of the heat balance is as following:

$$(C_A + C) \cdot dT/dt = P_0(t) - G \cdot (T(t) - T_0), \qquad (14)$$

where $T(t)$ and T_0 are the temperatures of the heating region and the environment (of the holder in fact), respectively. This equation is correct provided that the temperature scanning rate dT/dt is a few times smaller than the maximal $(dT/dt)_{max}$, which is limited by the thermal thickness of the sample and the size of the heated area as discussed in previous sections. For the sensor TCG-3880, the distance between the central heated area and the hot junctions of thermal couple is ~50 μm. The temperature measured by the thermopile is then ~10 ms delayed with respect to the heater current. Therefore the scanning rate must be less than $\Delta T/\tau_0$ where τ_0 = 10 ms. However, in the newly designed sensor, such limitation is removed because the hot junctions are now placed inside the heated area.

The heat flow $P_0(t)$ is determined by the electric current in the heater $I_H(t)$ and its resistance $R_H(T)$. The resistance $R_H(T)$ was calibrated in advance. The electric current in the heater was monitored in real time during its scanning simultaneously with the temperature difference $T(t) - T_0$ measured by the thermopile. The temperature dependence of the thermopile sensitivity S was calibrated by measuring the melting temperature of indium and other pure metals starting from different oven temperature T_0.

Thus there are three unknown parameters, G, C_A, and C, in Eq. (1). The parameter C_A was determined in advance for the empty cell. The heat transfer parameter G can be estimated according to $G = 4\pi r_0 \lambda_g$ and it can be measured simultaneously with C from a heating–cooling scan as following.

We are interested in the dependence $C(T)$ of a sample near a phase transition temperature T_c, where heat capacity C_c at cooling is not the same as C_h at heating. Consider a heating–cooling scan in the range from $T_c - T$ to $T_c + T$, where T is large enough for the observation of $C_c(T) = C_h(T)$ at least at the ends of the scanning interval far from T_c. Then, both functions $C(T)$ and $G(T)$ can be determined simultaneously as

$C(T) = (1/2)[P_{0,h}(t) - P_{0,c}(t)] \cdot |dT/dt|^{-1} - C_A$ and $G(T) = (1/2)[P_{0,h}(t) + P_{0,c}(t)] \cdot (T(t) - T_0)^{-1}$ at temperatures far from T_c. $P_{0,h}(t)$ and $P_{0,c}(t)$ denote the heat flows at heating and at cooling, respectively. Next, the $G(T)$ is approximated by a monotonous polynomial function and is extrapolated into the phase transition region, where the sample heat capacities $C_c(T)$ and $C_h(T)$ can be determined finally as follows:

$$(C_h + C_A) \cdot |dT/dt| = P_{0,h}(t) - [T(t) - T_0] \cdot G;$$

$$-(C_c + C_A) \cdot |dT/dt| = P_{0,c}(t) - [T(t) - T_0] \cdot G. \quad (15)$$

The scheme of the electronic setup is shown in Figure 5. The sensor (1) is connected through amplifiers (2) to the analog-to-digital and digital-to-analog converter (ADC–DAC) board (PCI-DAS64/M1/16 from Measurement-Computing™). A precision reference resistor R_{ref} (resistance of 100 Ω) is connected in series with the heater to measure the current through the heater. Data are collected at a rate of 5×10^4 samples/s. Two buffer differential amplifiers IC2 and IC3 (AD713J) are needed because the board requests low output impedance of the signal source if one wants to switch the inputs at high frequency. The preamplifier IC4 of type PGA204AP is used for the thermopile signal.

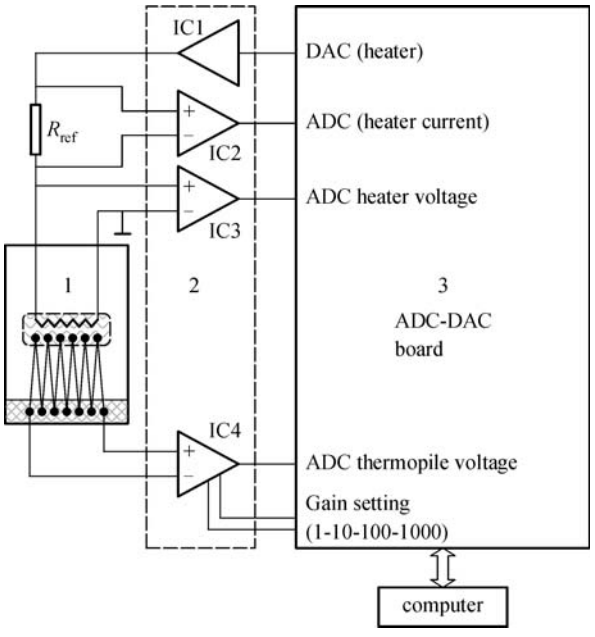

Figure 5 Scheme of the calorimeter. (1) sensor; (2) amplifier and (3) ADC–DAC board. Details are described in Section 4.1.

The methods described above have been used to study the crystallization and melting of poly(ethylene terephthalate) (PET) [21,22], poly(butylene terephthalate) (PBT) [29], isotactic polystyrene (iPS) [31], isotactic polypropene (iPP) [26–28], polyethylene (PE) [24,25], and submicron polyamide-6 (PA6) droplets in polystyrene/PA6 blends [30].

For the crystallization of polymers, a fully crystalline state with extended chain crystals is seldom reached owing to the long-chain nature of the polymers [50]. The morphology of the semicrystalline polymer is described by the stacking of crystalline polymers with multiply folded chains, localized fully amorphous domains, and intermediate motion-restricted rigid amorphous fractions [51,52]. During subsequent heating, the melting–recrystallization–remelting, the creation of secondary lamella, or the relaxation of rigid amorphous fractions are often considered for the description of the complex melting behavior of the semicrystalline polymers [53–60]. For several polymers such as PET, the issue is not finally resolved yet even though it was already studied since 1970 [61]. To exclusively investigate the melting of the originally formed crystals is difficult because recrystallization is a fast process and most experimental techniques applied so far do not allow fast heating in order to prevent recrystallization totally. Sauer et al. showed that the PET crystallized at low temperatures becomes liquid-like considering its viscosity at relatively low melting temperatures [62]. Robertson et al. [63] showed that recrystallization is ~2 orders of magnitude faster than isothermal crystallization at the same temperature using special temperature sequences in DSC experiments for PBT. To exclusively study the melting of the originally present crystals in a polymer sample consequently requires very high heating rates. Pijpers et al. extended the heating and cooling rate range of DSC to rates as high as 500 $K \cdot min^{-1}$ (Hyper DSC™) [64]. But for commercial PET, these rates are not high enough yet to prevent recrystallization.

The results of DSC measurements at heating rates up to 500 $K \cdot min^{-1}$ (8.3 $K \cdot s^{-1}$) for samples melt-crystallized at 210°C and 130°C are shown in Figure 6. For the PET sample melt-crystallized at 210°C (Figure 6(a)), a very complex melting behavior is observed. At the two lowest heating rates, two melting peaks at 260°C and 250°C and a broad shoulder around 240°C appear. The high-temperature melting peak decreases with the increasing of the heating rate, and disappears as a separate peak at the heating rate of 20 $K \cdot min^{-1}$. At higher rates, the shoulder at 240°C develops; finally, only one single peak is observed. The low-temperature peak at 240°C is hidden at low heating rates because of the continuous melting and recrystallization. Why we see two peaks at higher temperatures at low heating rates is not well understood, but all these peaks disappear at high heating rates. Obviously, there is no indication for any multimodal distribution in the melting temperatures, etc. For the crystallization temperature of 210°C, the rate of 200 $K \cdot min^{-1}$ (~3 $K \cdot s^{-1}$) is fast enough to reach some limiting curve shape. The crystals formed at 210°C do not recrystallize very fast. Therefore, the rate of 200 $K \cdot min^{-1}$ is fast enough to prevent recrystallization. The crystals formed at 130°C (Figure 6(b))

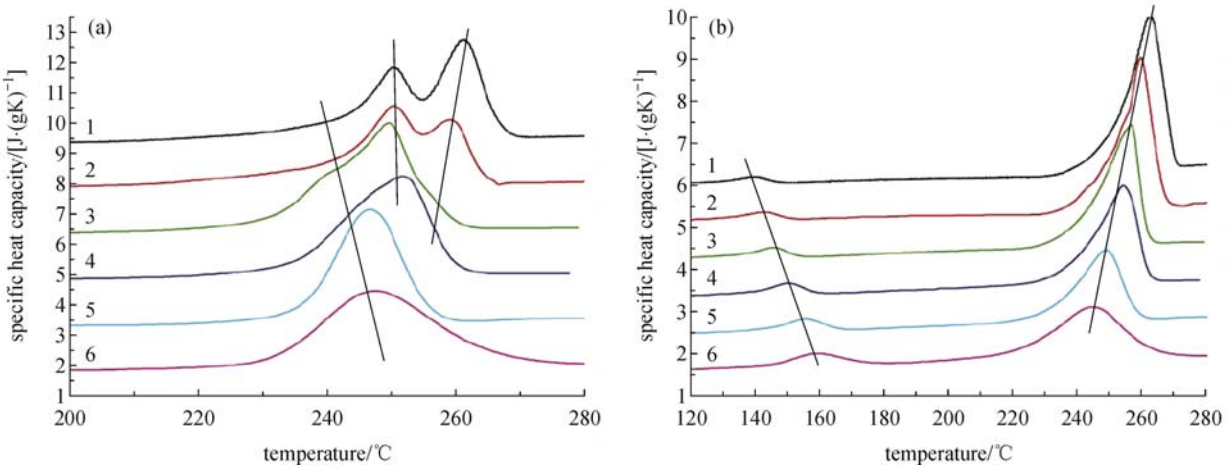

Figure 6 Temperature dependences of the specific heat capacity of 0.5 to 16 mg PET samples at the following heating rates, (1) 0.033 K·s^{-1} (2 K·min^{-1}) 16 mg; (2) 0.083 K·s^{-1} (5 K·min^{-1}) 16 mg; (3) 0.33 K·s^{-1} (20 K·min^{-1}) 6 mg; (4) 0.83 K·s^{-1} (50 K·min^{-1}) 6 mg; (5) 3.3 K·s^{-1} (200 K·min^{-1}) 0.5 mg and (6) 8.3 K·s^{-1} (500 K·min^{-1}) 0.5 mg. The samples were crystallized at (a) 210°C and (b) 130°C for 1 h. The curves are vertically shifted and the straight lines are guides to the eyes only.

are less stable. Therefore, even at 500 K·min^{-1}, two well-separated peaks are observed. But the increasing low-temperature peak and the shift of the second melting peak towards lower temperatures with increasing heating rate strongly support the melting–recrystallization–remelting model for this sample, too. Obviously, the rate of 500 K·min^{-1} is not fast enough to prevent recrystallization.

In order to increase the heating rate even more, we used the chip calorimeter described in the experimental part. The PET sample of 360 ng was molten at 340°C for a very short time to minimize degradation of the sample. During heating and cooling at 2700 K·s^{-1}, the sample was subjected to temperatures above 300°C for 30 ms only. After isothermal cold crystallization, the sample was quenched again below glass transition at 30°C. The quenching rate was 10^4 K·s^{-1}. The measurements were then performed at different scanning rates. The melting curves and the subsequent cooling curves at the same rates are shown in Figure 7. The appearance of dramatic changes in the shape of the melting peaks depends on the heating rate. When cooling, no crystallization occurs and the glass transition of the amorphous PET is seen. For the two lowest rates, two separate melting peaks are observed. The high-temperature peak decreases with increasing heating rate and shifts to lower temperature as for in DSC measurements (see Figure 6(a)). At 1100 K·s^{-1}, only a shoulder remains at the high-temperature flank. Even at the rates of 2700 K·s^{-1}, the melting peak shows a slight shoulder. It may be explained by the recrystallization during the scan or a broad distribution in the crystal stability (melting points), which may exist for the crystals initially formed at 133°C.

The similar situation is found for the crystallization of iPS.

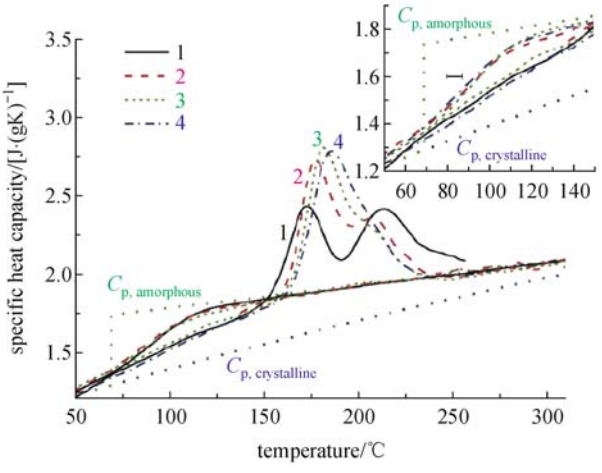

Figure 7 Temperature dependences of the specific heat capacity of 360 ng PET sample crystallized at 133°C for 1 h on heating and subsequent cooling. The measurements were performed at the scanning rates:(1) 150 K·s^{-1} (9000 K·min^{-1}; solid line); (2) 550 K·s^{-1} (33,000 K·min^{-1}; dashed line); (3) 1100 K·s^{-1} (66,000 K·min^{-1}; short dashed line) and (4) 2700 K·s^{-1} (162,000 K·min^{-1}; dashed-dotted line). The inset shows the curves in the glass transition range. The curves for the completely amorphous and crystalline PET according to Ref. [100] are shown by dotted lines.

The iPS sample melt-crystallized at 170°C (Figure 8(a)) shows again a complex melting behavior. At the two lowest heating rates, three peaks appear at 180°C, 205°C, and 220°C, respectively. The high-temperature melting peak decreases as the heating rate increases. At 500 K·min^{-1}, all three peaks merge to one broad melting peak ranging from 195°C to 240°C. Obviously, there is no direct indication for any

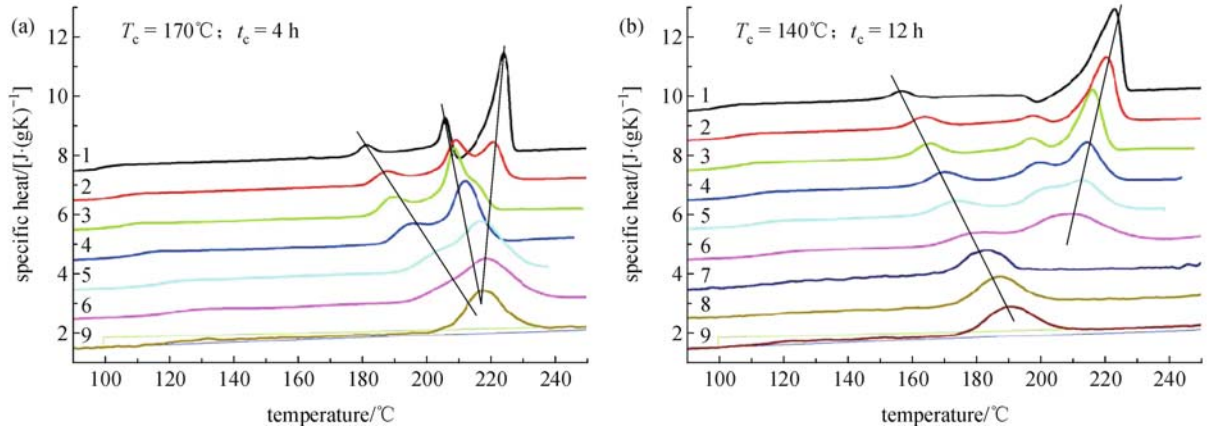

Figure 8 Temperature dependences of the specific heat capacity of 400 ng to 4 mg iPS samples at the following heating rates: (1) 0.16 K·s^{-1} (10 K·min^{-1}; 4 mg); (2) 0.83 K·s^{-1} (50 K·min^{-1}; 4 mg); (3) 1.6 K·s^{-1} (100 K·min^{-1}; 0.5 mg); (4) 3.3 K·s^{-1} (200 K·min^{-1}; 0.5 mg); (5) 6.6 K·s^{-1} (400 K·min^{-1}; 0.5 mg); (6) 8.3 K·s^{-1} (500 K·min^{-1}; 0.5 mg); (7) 100 K·s^{-1} (6000 K·min^{-1}; 400 ng); (8) 250 K·s^{-1} (15,000 K·min^{-1}; 400 ng) and (9) 500 K·s^{-1} (30000 K·min^{-1}; 400 ng). The samples were crystallized at (a) 170°C and (b)140°C for 12 and 4 h, respectively. The curves are vertically shifted and the straight lines are guides to the eyes only.

multimodal distribution in melting temperatures, etc. for the crystallization temperature of 170°C. But the observed peak is very broad and probably the superposition of multiple peaks. The crystals formed at 140°C (Figure 8(b)) are less stable. Even at 500 K·min^{-1}, two well-separated peaks are observed, indicating recrystallization. But the increasing low temperature peak and the shift of the second melting peak towards lower temperatures at increasing heating rate strongly support the melting–recrystallization–remelting model for this sample, too. Obviously, 500 K·min^{-1} is not fast enough to prevent recrystallization. With the chip calorimeter, there is only one peak that can be seen at heating rates above 6000 K·min^{-1} (100 K·s^{-1}) for both samples. For the sample crystallized at 170°C, the broad peak observed at 500 K·min^{-1} becomes significantly smaller, indicating the occurrence of recrystallization even at 500 K·min^{-1}.

The peak temperature of the low melting peak of PET and iPS depends strongly on the heating rate; this peak shifts to higher temperature as the scanning rate increased. This is because the peak temperature equals to the temperature where the difference between melting and recrystallization rate is maximal. At slightly higher temperatures when the heat flow is close to zero, a steady-state regarding melting and recrystallization is established. At low rates, as long as a second melting peak is observed, the maximum is not at all related to some maximum in the lamella thickness distribution as considered for the construction of a Hoffman–Weeks plot [65]. A detailed discussion is also presented by Yamada et al. [66,67]. Very high heating rates are needed to prevent recrystallization during the melting of PET and to obtain a meaningful melting temperature for the lamellae formed at isothermal crystallization. Under the conditions of fast heating, superheating has to be considered, too. From a technical point of view alone, it is therefore very questionable if a Hoffman–Weeks extrapolation can yield correct values for the equilibrium melting temperature of polymers.

Superheating and supercooling are associated with the nucleation of the new phase inside the primary one during a first-order phase transition (e.g., solid-liquid transition). The study of the melting transition can be useful for the understanding of the nature of the crystalline phase as well. The melting process of crystals is usually initiated at heterogeneous sites such as grain boundaries and free surfaces. Provided that the heterogeneous nucleation can be avoided, the crystals can be superheated significantly above the equilibrium melting temperature. The actual melting process then starts at a temperature T_m above T_0. Generally, superheating can be realized at a sufficiently large heating rate $R = dT/dt$ even in the presence of heterogeneous sites. The superheating magnitude $\Delta T = T_m - T_0$ depends on the kinetics of the melting process and increases with the heating rate. Nevertheless, there is a critical temperature T_c^m, above which a solid cannot be heated without transforming into a liquid [68–74]. A crystal becomes unstable at temperatures above T_c^m and a catastrophic melting process will be initiated.

The nature of the upper limit of the superheating T_c^m is not completely understood at present. Several models for the crystal instability at critical superheating were proposed [68–74]. These thermodynamic or kinetic models predict $(T_c^m/T_0 - 1)$ to be varying from 0.2 to 0.38, but it is significantly higher than the typically experimentally observed value $(T_c^m/T_0 - 1) \sim 0.1$ [74]. In order to verify the different

approaches to determine the superheating limit, kinetic experiments on superheating in a broad range of heating rates are required.

The crystalline amorphous interface in the polymers is rather fractal than flat on the scale ranging from a few nanometers to a few micrometers [75–78]. Therefore, heterogeneities play an important role in the melting process of polymers. Nevertheless, polymers can be superheated significantly above T_0^* at sufficiently fast heating rate [66,79–82]. The melting kinetics and superheating in polymers is not understood at present. Generally, at sufficiently low heating rates (e.g. at $\sim 1\,\mathrm{K\cdot s^{-1}}$), the melting process is often accompanied by recrystallization and the shape of melting curves can be very complicated as shown above [21,22,29,75,83]. Therefore, the first experimental question arises: how to determine the melting temperature $T_m(R)$ in the presence of recrystallization? Next, is it possible to measure $\lim_{R\to 0} T_m(R)$ with a reasonable accuracy in the presence of recrystallization? This is important because it is required as a reference point for superheating measurements. As we have shown, the recrystallization for several polymers can be avoided at heating rates above $10^3\,\mathrm{K\cdot s^{-1}}$. Rates up to $10^5\,\mathrm{K\cdot s^{-1}}$ are required for the measurement of the critical instability of superheating in polymers as will be shown below. At such heating rates, the sample should be thin enough (~10 μm) due to heat transfer limitations [45]. Consequently, the experimental technique should be quite sensitive for measuring samples in the nanogram range. Last but not the least, the initial sample state must be definite and reproducibly prepared. For example, the sample should be reproducibly quenched from the molten state to a crystallization temperature T_c, be isothermally crystallized at T_c during a definite crystallization time t_c, and be heated with a definite rate to the melt. Therefore, we need a sample processing system with possibility to scan temperature $T(t)$ at ultrafast rates with at least millisecond resolution. The cooling process should be controlled as well as the heating. For these reasons, the sensitive ultrafast scanning calorimeter described above is the key step towards the study of the superheating of polymers.

First of all, the position of the first endothermal peak T_p of the melting curve cannot be used for T_m measurements in polymers because the melting process is accompanied by recrystallization and remelting. Therefore, T_p is determined not only by the melting of the original crystals but also by the recrystallization process. The recrystallization is initiated just after the start of melting. Then, for a correct recrystallization independent definition of T_m, it is reasonable to use just the melting onset. Furthermore, it is the only way to define T_m in the case of a strong recrystallization-remelting process. Another reason to use such a definition is that a possible apparatus thermal lag can cause the broadening of the melting peak. And the maximum of the melting curve can be shifted to higher temperatures. This shift increases with the increasing of the sample mass and specific enthalpy of fusion related to the melting transition. On the other hand, the position of the melting onset is basically independent of the lag. Next, even if the recrystallization is avoided, the position of a melting curve maximum can be dependent on other reasons not directly related to the superheating. The melting onset can be determined using the intersection of the extrapolated heat capacity curve before melting and the linear fit to the rising flank of the first melting peak. Although the melting onset is smeared due to the recrystallization process, we have found that the extrapolated melting onset can be detected with good reproducibility of about ±1 K. Consequently, the error of the T_m measurements was determined by the uncertainty of the extrapolated melting onset detection [25].

Superheating of iPS, PBT, PET, and iPP with different abilities of recrystallization are studied in a broad range of heating rates [25]. The typical result is shown in Figure 9. For at least the following observations, we can safely say that

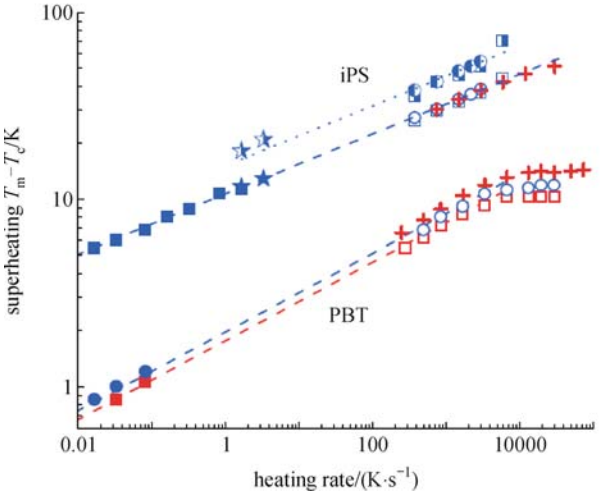

Figure 9 Rate dependence of superheating $\Delta T = T_m - T_c$ measured by DSC for 5 mg iPS samples (filled symbols) and 0.8 mg iPS samples (stars) as well as by fast scanning calorimeter for 150 ng iPS samples and 170 ng PBT samples (empty symbols). The dependence curves of 40 ng iPS samples and 32 ng PBT samples (crosses) are also shown. The iPS samples were crystallized at 205°C for 16 h (squares) and 1 h (circles and crosses). respectively. The PBT samples were crystallized for 15 min at 200°C (circles) and 180°C (squares and crosses). respectively. Dashed lines correspond to the power law $\Delta T(R) = AR^{\beta}$ with β = 0.16 and A = 10.6 K for the iPS and with β = 0.21 and A = 1.95 K and 1.75 K for the PBT at T_c = 200°C and 180°C. respectively. The shift of the melting peak $\Delta T_{max} = T_{max} - T_c$ for iPS is shown by semifilled symbols.

superheating does not come from the thermal lag of the apparatus but from the measurement of the intrinsic properties of samples studied. The observations are listed as following. (1) Samples of different masses, i.e. 150 ng and 40 ng for iPS as well as 170 ng and 32 ng for PBT, were measured; but the superheating is independent of the sample mass as shown in Figure 9. (2) For the same sample on the same sensor, the superheating is determined by the annealing temperature T_c and annealing time t_c. This is particularly clear for iPP, whose recrystallization–remelting effect is very strong [25]. (3) At high heating rates, the dependence $\Delta T(R)$ tends to saturation. Such behavior is just opposite to what was expected due to the apparatus thermal lag. The situation may be resulted from the fact that the sample we used for very high rate scanning is only a few micrometers. In such case, the surface effect is no longer neglectable because the surface nucleation can substantially increase the crystallization rate compared to the rate in large samples.

In the studies discussed above, strong superheating $\Delta T/T_m \sim 10\%$ is observed in slow, moderate, and fast crystallizing linear polymers. The increment $\Delta T = T_m - T_c$ is an appropriate definition of superheating in the linear polymers, where T_m is the melting onset and T_c is the crystallization temperature. The heating rate dependence of the superheating in the linear polymers is described by the power law:

$$\Delta T(R) = AR^{\beta}. \tag{16}$$

The parameter A is in the range of 2 to 10 K for different polymers; it depends on the annealing temperature T_c and even on the annealing time interval t_c as in the case of iPP. The exponent β is in the range of 0.16 to 0.21 for different polymers and depends only slightly on T_c and t_c. Eq. (16) is, in some cases, satisfied for 6 orders of magnitude in the heating rate. The dependence $\Delta T(R)$ is a straight line in the double logarithmic plot. Within this plot, we have found a quasi-equilibrium melting temperature $T_0^* = \lim_{R\to 0} T_m(R)$ equal to T_c. This result is not surprising for semicrystalline materials, in which heterogeneous melting can take place at the interface between the amorphous and the crystalline phases. Therefore, the melting can start at a temperature just above T_c. Nevertheless, the melting process can be slowed down due to an energy barrier retarding the crystalline amorphous interface movement. Thus for example, at the heating rate of $10^{-2}\,K\cdot s^{-1}$, the melting onset in PBT and iPS is observed at 0.7 K and 5 K above T_c, respectively, as shown in Figure 9. Apparently, the energy barrier in the slow crystallizing polymer iPS is larger than that in PBT as well as in PET and iPP.

The reason why the linear polymers can be superheated significantly above T_c and on the superheating critical limit can be explained by the local stress generated at heating near the crystalline amorphous interfaces. It predicts that β equals to ~0.25, in good agreement with experiments. The stress is created due to the thermal expansion gradients existing near the interfaces. These gradients are inherent in the semicrystalline polymers because the thermal expansion of the amorphous phase is considerably larger than that of the crystalline one.

4.2 Isothermal calorimeter

Besides measuring the heat capacity during the fast cooling or heating, the fast scanning calorimeter can also be used to prepare samples with certain thermal history that is needed for the study of the isothermal process (e.g., isothermal crystallization, reorganization, or chemical reactions) just after the fast cooling or heating. Based on the fast scanning calorimeter, an isothermal calorimeter is built with a time resolution better than 10 ms.

Figure 10 shows the melting, cooling, and crystallization of a polycaprolactone (PCL) sample of ~100 ng on the sensor TCG-3880. We can see an almost constant time lag of ~10 ms between the temperature change and the heating power. This is an indication of the quasi-static heating and cooling conditions, which is predicted by Eq. (15). At the end of the cooling, the heater power equals to zero. Because of the ballistic cooling at the very end of the cooling scan, the sample temperature approaches the oven temperature at slower rate. If we zoom in the temperature signal (inset in Figure 10), we can see some increase of the temperature at the beginning of the isotherm. This is due to the crystallization of the PCL sample, which is an exothermic process. To obtain the heat flow rate to the surroundings from the measured

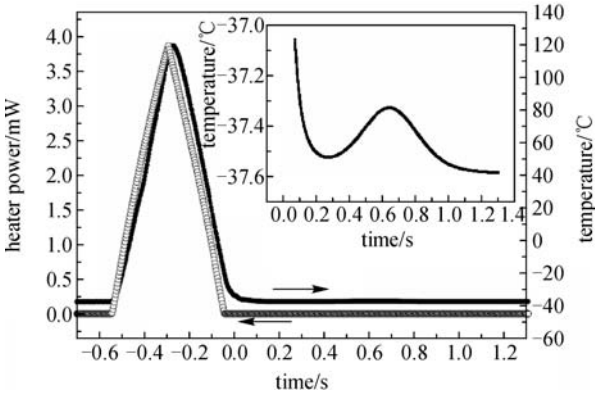

Figure 10 Melting and isothermal crystallization of a PCL sample (~100 ng). Heating-cooling rate was $700\,K\cdot s^{-1}$; the oven temperature was −38°C. Inset shows small temperature change dues to crystallization.

temperature increase, one can make use of the almost linear dependency between the heater power and the temperature as seen in Figure 10. This is because power losses are at the first approximation proportional to the temperature difference between the sample and the surroundings.

This experiment clearly proved that the performance of the calorimeter based on the sensor TCG-3880 followed the isothermal processes. When temperature is below the maximum crystallization temperature, the crystallization rate decreases dramatically until it reaches zero at the glass transition temperature. At low crystallization rates, the heat flow rate from the sample to the surroundings also decreases and reaches the noise level. To follow the isothermal process under such conditions, we can measure the heat capacity, which is decreasing with the increasing of the crystallinity, to follow the process of crystallization. To measure the heat capacity, one can apply a small oscillating voltage to the heater to generate an oscillating power of a few microwatts and detect the amplitude of the temperature oscillations on the second harmonic of the voltage [84] as commonly performed in AC calorimetry. As generally known from AC calorimetry, the proper choice of the modulation frequency is important if one wants to measure the absolute values of heat capacity [85,86]. However, to study the crystallization kinetics, it is enough to measure relative changes in heat capacity; therefore we can neglect all the non-trivial calibrations and corrections. Choosing small temperature amplitudes allows keeping conditions of linear response. Apparent heat capacity can then be obtained from the ratio of power and temperature amplitudes.

The basic electronic setup is the same for the scanning calorimeter. A Stanford Research DS340 programmable arbitrary function generator was used to drive the current through the heater in accordance to the desired time-temperature profile. The function was generated by a computer and downloaded to the DS340 via computer interface. A model 7265 lock-in amplifier from EG&G Instruments (now Signal Recovery) was utilized for the measurement of the AC signal. The lock-in amplifier measured the amplitude of the temperature oscillations at the second harmonic. Heater voltage amplitude was 30 mV, corresponding to the power amplitude of ~1 μW. The voltage at the thermopile was ~30 μV, corresponding to temperature amplitude of ~30 mK.

Moreover, one can perform "scan" and "oscillating" measurements simultaneously. Then the generator output of the 7265 lock-in amplifier was connected in parallel to the DS340 output. However, it was not possible to synchronize the start of data acquisition of the 7265 with the beginning of the pulse of the DS340 because of problems in both devices. Therefore, a PXI-6120 board from National Instruments is used. This board provides four high-speed (1 Ms/s), simultaneous analogous sampling channels. The DAC output is programmed to provide a heating pulse superposed by an AC modulation. The other three channels are used to measure the current (reference resistance voltage), heater voltage, and thermopile voltage, respectively. This electronic setup is shown in Figure 11.

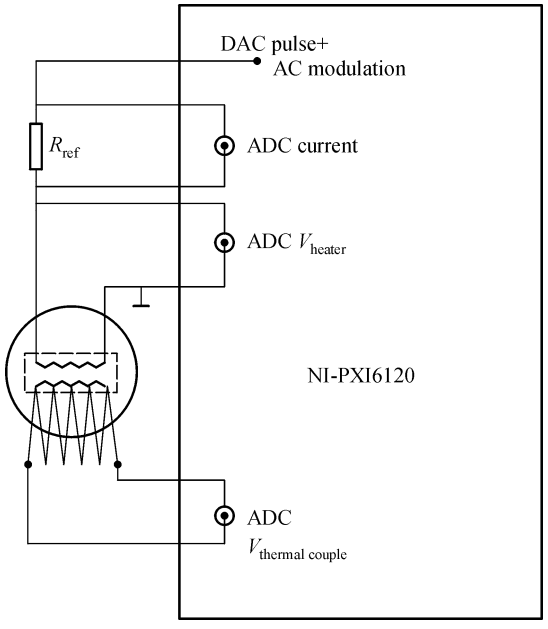

Figure 11 The electronic scheme of the isothermal calorimeter using NI-PXI6120 board.

For relatively fast crystallization, the heat flow rate due to the enthalpy change is large. Then we can observe a crystallization peak in the temperature (see Figure 10). In the time interval between the end of the cooling and the local maximum of the overheating, the crystallinity reaches roughly half of its end value at the actual temperature. We call this time "crystallization half-time". The reciprocal is a measure for the overall crystallization rate. At crystallization half-times longer than 10 s, the temperature signal decreases below the noise level. To follow the crystallization at slower rates, we have to switch to heat capacity measurements as described above.

A relatively high oscillating frequency was chosen to get better resolution in time and to follow the crystallization almost from the very beginning. The "crystallization half-times" obtained by the two methods, total heat flow and heat capacity, are quite similar (see Figure 12). The time of the maximum of the crystallization rate (the local maximum in the temperature signal), t_{max}, corresponds to the time in good approximation when the heat capacity approaches half-way of the total decrease, $t_{0.5}^{c_p}$.

By using the fast isothermal calorimeter, we have studied

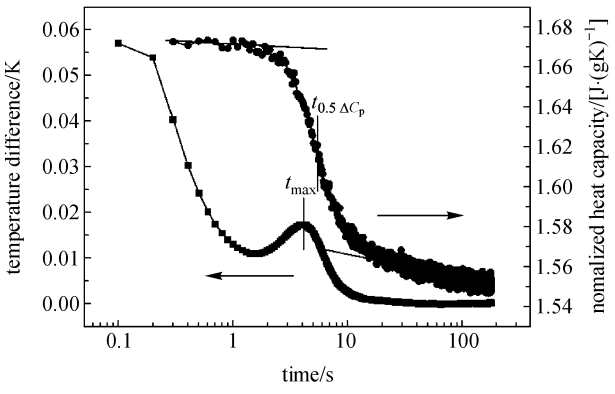

Figure 12 Different modes of the PCL crystallization kinetics measurements. Heat frequency $2f$ was 140 Hz and the oven temperature was −54°C. The curves represent the average over 128 measurements of the oscilloscope.

the isothermal crystallization of PCL, PE, iPP, PBT, and some iPP nanocomposites and blends [23,26,28,33]. For PCL, the crystallization half-time shows a typical bell-shaped temperature dependence; for iPP and PBT, a bimodal crystallization rate as shown in Figure 13 is found, probably owing to the polymorph properties of iPP [28]. Why a similar curve is observed for PBT is not yet understood [29]. For PE, the crystallization is so fast that it starts even during the cooling. So far, the temperature of the maximum crystallization rate for PE is yet unknown.

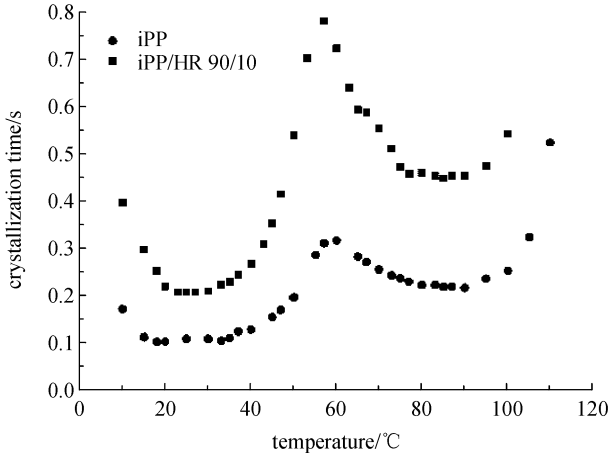

Figure 13 Crystallization time of iPP and iPP/HR 90/10 film after fast cooling from the melting inside the chip isothermal calorimeter.

4.3 AC calorimeter and differential AC nanocalorimeter

With the ultrafast calorimeter, we can prepare samples far from equilibrium and measure their physical properties. But often one would prefer to measure the thermal properties of small samples at or at least close to thermodynamic equilibrium. This can be achieved by a combination of the chip calorimetry and the AC calorimetry. While on scanning the relation between the scanning rate and the relevant time scale for the molecular processes at glass transition is not easily established [87,88] for the AC calorimetric measurements, the frequency of the temperature oscillation can be straightforward linked to the dynamics of the molecular processes under investigation. At glass transition for the maximum of the frequency-dependent imaginary part of complex heat capacity, the relation $\omega\tau = 1$ holds, where $\omega = 2\pi f$ is the angular frequency of the perturbation and τ is mean relaxation time.

As common in AC calorimetry, a small periodic heat flow with amplitude P_0 is provided to the heater of the sensor and the resulting complex temperature amplitude T_A is measured. The measurements are performed at slow scanning or at constant bath temperature. Owing to the small size of the heated area, at a large distance compared to the radius r_0, the thermal oscillations exited in the gas are closely spherical waves: $T_g(t,r) \sim \exp(i\omega t - k_g r)/r$. The complex valued wave number k_g is given by the dispersion law for the thermal waves: $k_g^2 = i\omega\rho_g c_g/\lambda_g$, where c_g and λ_g are the specific heat capacity per unit of volume and the thermal conductivity of the gas, respectively. The heat loss through the gas can be described by the heat exchange coefficient $G = 4\pi r_0 \lambda_g$. Solving the Fourier heat flux equation for such a system, one gets the temperature modulation amplitude of the heated membrane area:

$$T_A = \frac{P_0}{i\omega C + G}. \tag{17}$$

Therefore, the apparent heat capacity $C_A = P_0/(i\omega)T_A$ equals to $C + G/(i\omega)$. The term $G/(i\omega)$ in the apparent heat capacity describes the heat loss through the surrounding gas. Further contributions to the apparent heat capacity are determined as follows: the effective heat capacity of the sample with a finite sample thickness d_S is given by $C_S \tanh \alpha_S/\alpha_S$, where the effective thermal thickness α_S of the sample is defined as the thickness d_S times thermal wave number k_s $d_s k_s = d_s\sqrt{i\omega\rho_s c_s/\lambda_s}$ for the substance. For thin films, $\alpha_S \ll 1$ and then the factor $\tanh \alpha_S/\alpha_S$ equals to one with high precision up to 10 kHz. The size of the heated area of the sensor is frequency dependent and becomes smaller with higher frequencies. Thus, the apparent addenda heat capacity can be described by Eq. (10) to Eq. (12).

With the sensor TCG-3880, Minakov developed the first chip AC calorimeter and successfully studied the magnetic phase transition of a 3.8 μg sample of ruthenium-doped $CeFe_2$

in magnetic fields up to 8 T and in the temperature range of 20 to 280 K [89]. The sensitivity of this system is ~10 nJ·K^{-1} at room temperature. The sensitivity of this calorimeter should be improved if we want to study even smaller systems (e.g., glass transition of polymer confined into a few tenths of nanometers). As will be shown below, by a differential design, we achieved sensitivity in the pico-Joule per Kelvin range, allowing to measure samples of ~1 ng. Consequently, the limit for film thickness is in the range of 1 nm [37]. Because of the small total heat capacity (addenda and sample), not only a high sensitivity is achieved but the AC measurements at relative high frequencies are possible, too [84]. The calorimeter allows heat capacity measurements in the frequency range of 1 to 1000 Hz.

For the difference of the thermopile signal amplitudes $\Delta T_A = \Delta T_{A0} - \Delta T_{AS}$ an empty sensor ΔT_{A0} and a sensor with a sample ΔT_{AS}, the following equation holds:

$$\frac{i\omega\Delta T_A}{P_0} = \frac{1}{C_0(\omega) + G/(i\omega)} - \frac{1}{C_0(\omega) + C_S + G/(i\omega)} \approx \frac{C_S}{[C_0(\omega) + G/(i\omega)]^2}, \quad (18)$$

where the term C_S was neglected with respect to C_0 assuming $C_S \ll C_0$. With an effective heat capacity of the empty cell $\widetilde{C} = C_0(\omega) + G/(i\omega)$, one gets $i\omega\Delta T_A/P_0 \approx C_S/\widetilde{C}^2$. In this formula, two identical sensors are assumed.

When there is asymmetry between sensors, $i\omega\Delta T_A/P_0 \approx [C_S + \delta C_0 + \delta G/(i\omega)]/\widetilde{C}^2$. The temperature amplitude is given by the voltage amplitude at the thermopile U divided by the thermopile sensitivity S. For the case of two empty sensors, the differential thermopile signal is denoted by ΔU_0 and for the case with the sample ΔU. In terms of the measured quantities, the heat capacity of the sample for the non-ideally symmetric system is then given by:

$$C_S = i\omega\widetilde{C}^2(\Delta U - \Delta U_0)/(SP_0). \quad (19)$$

Eq. (19) is valid for thin (submicron) samples. If the sample thickness increases, the factor $\tanh \alpha_S/\alpha_S$ has to be taken into account.

The electrical scheme of the device is shown in Figure 14. The heaters on the chips are driven by an alternating current at frequency $\omega/2$ from the oscillator of the lock-in amplifier. This results in an oscillating power at frequency ω. The amplitude and phase of the resulting oscillating temperature at frequency ω are measured with the surrounding thermopile using a digital lock-in amplifier (Model 7625 from Signal Recovery). The oscillator voltage is applied to the two sensors and a known constant resistor in series. The applied power is calculated from the voltage over the known resistor measured

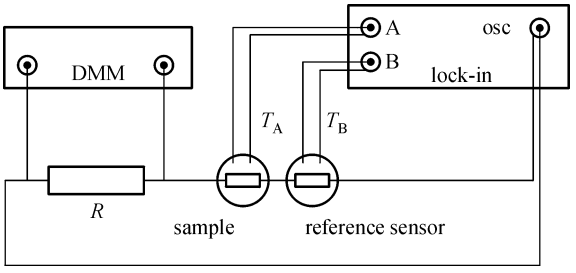

Figure 14 Schematic picture of the electric setup. The usage of the internal generator of the lock-in amplifier results in better phase stability. The differential signal A-B of the thermopiles is analyzed and further processed. The voltage over the known resistor R is measured with a digital multimeter in order to calculate heater power. All components are controlled by a computer.

with a digital multimeter (PREMA 6001) or with an extra ADC input of the lock-in amplifier, which takes the oscillator voltage and the internal resistance of the oscillator into account. Both sensors are placed adjacent in a thermostat at temperature T_B. Measurements are carried out either at a single frequency with the temperature changing continuously (temperature scans) or at different frequencies with constant temperature (frequency scans). In the later case, the emperature can be changed stepwise. A self-made computer program using Labview^R was used to control the instruments.

Depending on the surrounding gas and sample thickness, the available frequency range is between 1 Hz and 1 kHz. The heater power per sensor is ~10 to 50 μW, resulting in a temperature oscillation amplitude and a temperature bias of less than 1 K. The frequency of the maximal sensitivity depends on the thermal conductivity and the heat capacity of the surrounding gas. For nitrogen at ambient pressure, the maximal sensitivity is observed between 10 Hz and 100 Hz. For lower frequencies, the losses through the gas dominate. Reducing the losses by lowering the pressure in the frequency range can be extended to lower values. For higher frequencies, the thermal gradient in the heated membrane and within the sample will become too large, resulting in large inhomogeneity and instability.

The differential AC chip calorimeter can be specific heat spectroscopy for polymers [37,90–93], liquid crystals [94], and other glass forming materials [35]. For example, the glass transition of polystyrene (PS) films is from 50 to 4 nm [36, 37]. The films are produced by spin coating the polymer solution onto the sensor. The thickness is assumed to be same as the thickness of film spin-coated onto the flat silicon wafer under identical conditions (identical polymer concentration and identical spin rate). In Figure 15, data from a polystyrene film of 15 nm thickness are shown. Frequency sweeps from

0.6 to 1280 Hz are performed and the temperature is changed stepwise from 323 K to 423 K in steps of 5 K (only 80 Hz is illustrated). Here, we do not determine the heat capacity from measured signals. Nevertheless, the glass transition temperature and relative changes of the signal are easily detected. The empty measurement of the system gives an additive term that is usual at least one order of magnitude lower than the signal of the sample. Therefore, contributions from asymmetry only slightly change the overall picture in such a small temperature range and do not affect the glass transition temperature determination. From the real part of the measured thermopile signal, the frequency-dependent glass transition temperature is determined as the half-step temperature. The tangent construction for the determination is indicated in the figure. Also in the phase, a peak at the glass transition is found as commonly for complex heat capacity. The half step of the real part and the maximum in phase are at the same temperature position. There is an underlying step in the phase that is proportional to the real part. The phase signal is corrected by subtracting this contribution as described in Ref. [95]. For the 15 nm sample, the peak in the phase is detectable and can be used to determine the glass transition temperature in the range of 20 to 320 Hz, while the step at the glass transition can be evaluated in the frequency range from 0.6 to 1280 Hz. Both values (peak temperature and temperature at half-step height) are in good agreement within the error limit of ±3 K.

With this calorimeter, the thickness dependence and the glass transition temperature for films of thickness down to 4 nm are studied at the frequency of optimum sensitivity. The

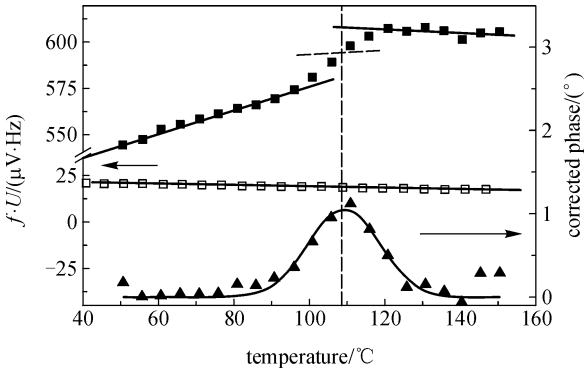

Figure 15 Corrected phase angle (solid triangles) and signal amplitude times frequency for a polystyrene film of the thickness of 15 nm (solid squares) and for an empty sensor (open squares) for a frequency of 80 Hz. The measurements are performed isothermally with 5 K steps. The tangent construction for determining the dynamic glass transition temperature from the real part is shown. A peak in the phase appears in the glass transition range as expected.

second heating–cooling cycle is evaluated to avoid influences of sample preparation such as the evaporation of solvent residues. The glass transition temperature is determined as the half-step temperature using the tangent construction as shown above. The results are shown in Figure 16 and Figure 17. No changes in temperature position or the deviation from the WLF behavior [96] for the measured film thicknesses were found. Poly(methyl methacrylate) (PMMA) films from 400 to 10 nm [97] and blend of PS with poly(phenyl oxide) (PPO) from 300 to 5 nm are also studied in the same way. No shift in

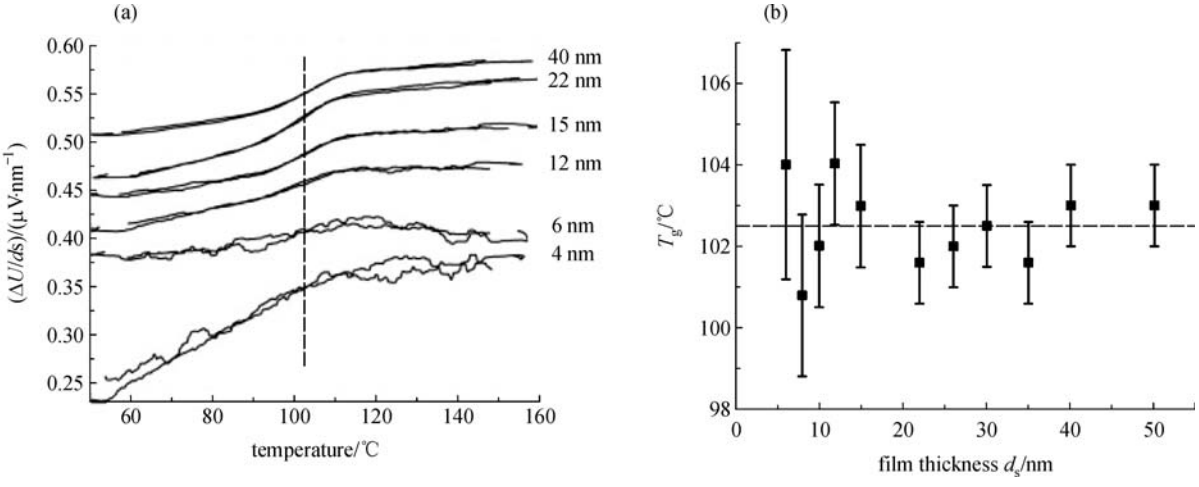

Figure 16 (a) The normalized AC calorimetric response $\Delta U/d_s$ as a function of the temperature for six different film thicknesses d_s and (b) the film thickness dependence of the glass transition temperature at 40 Hz for the series of polystyrene films from 50 to 8 nm. The 4-nm-thick film shows a kink in the same range as indicated by the line in A. However, the data are not shown in this figure because no clear step is found.

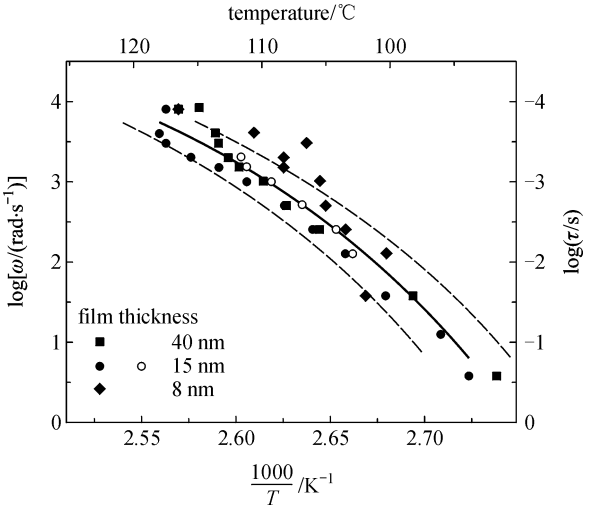

Figure 17 Arrhenius plot for the glass transition of the polystyrene film of different thickness. The solid symbols are from the half-step temperature of the real part and the open circles from the peak in the phase for a film thickness of 15 nm. The curve is a WLF fit $\left(\log\omega = \log\Omega - \frac{B}{T-T_0}\right)$ [96] to the data of 15 nm obtained from the real part with the parameter $\log\Omega = 8\ \mathrm{rad\cdot s^{-1}}$, B = 250 and T_0 = 333 K. The dashed lines indicate the error limits of ±3 K.

the glass transition temperature depending on the film thickness is observed, which is similar to the results presented by Efremov and Allen [9,16]. For the film thickness in the range of 50 nm down to 4 nm, other studies report glass transition temperature reductions of more than 25 K for polystyrene of similar molecular weight [98]. This reduction is significantly larger than the uncertainty of the glass transition temperature determination by the AC calorimetric measurements. Unfortunately, the present setup does not allow the measurement at lower frequencies as mandatory for a direct comparison with the data presented by Fakhraai and Forrest [99]. To extend the frequency range to lower frequencies, measurements should be performed at reduced pressure. Necessary setup is under construction and hopefully will allow the measurement at least down to the frequencies of 0.05 Hz. In this case, this calorimeter may help to gain a deeper insight into the dynamic behavior of supported thin films in a wider range of timescales.

5 Summary

The strategy we applied to realize ultrafast cooling is to use a tiny sample placed on a point-like heater of several tenths of microns and to run in the low thermal inertia gas atmosphere. Commercial sensors from the Xensor Integration, NL, which are fabricated on the submicron silicon nitride film, can be used to set up the fast cooling chip calorimeter. The maximum controllable cooling and heating rates can be increased by decreasing the size of heated area if we suppose the sample is thin enough. Therefore, the sensor XEN-3973 with a radius of heated area of ~20 μm can be applied to the thermal processing and simultaneous measurements at scanning rate up to $10^6\ \mathrm{K\cdot s^{-1}}$. Besides the possibility of fast scanning, the calorimeter are very sensitive. They are successfully applied to the study of the complex melting and crystallization of a wide range of polymers (e.g., PET, PBT, PE, iPP, iPS, and polyamide) with the sample mass down to ~30 ng. Based on the fast scanning calorimeter, we have built the isothermal calorimeter and the differential AC calorimeter. The isothermal calorimeter has the time resolution in milliseconds that can be used to study the isothermal crystallization kinetics of fast crystallizing polymers, such as PAL, iPP, and PE. The differential AC calorimeter has a very high sensitivity (~50 $\mathrm{pJ\cdot K^{-1}}$) and a wide modulation frequency range (10^{-1} – 10^3 Hz). The differential AC calorimeter has been used to study the glass transition of PS, PMMA, and PS/PPO blend confined into thin film down to a few nanometers. No thickness dependence of glass transition temperature and no significant deviations from the WLF behavior are found for these polymers. This finding is in agreement with the results from fast scanning calorimetric experiments reported by Efremov and Allen [9,16] and is contrary to many other studies that report strong thickness dependence.

To further increase the performance of fast cooling calorimeter and isothermal calorimeter, we can further decrease the size of the heated area; however, this will make difficult of the fabrication of the thermopile and more importantly, of the sample preparation as well. Another possibility is to decrease the thickness of the silicon nitride membrane without destroying its mechanical integrity. Therefore, the addenda heat capacity and the time constant of the isothermal calorimeter can be decreased. Decreasing the thickness is also important if we want to increase the upper limit of the frequency range of measurement in the AC calorimeter. However, to extend to lower frequency, measurements should be performed on the reduced gas pressure.

Acknowledgements The methods described here were developed by A. Minakov, S. Adamovsky and H. Huth. The authors gratefully acknowledge the support and stimulating discussions with them. The development was financially supported by the German Science Foundation (DFG) through several grants (Schi 331/7-14). This work is financially supported by the National Natural Science Foundation of China (Grant Nos. 20504014, 50533020, and 20874045) and the National Basic Research Program of China (No. 2007CB925101). D. Zhou thanks the Alexander von Humboldt (AvH) Foundation for providing a fellowship enabling him to stay in Schick's group for 18 months.

Dongshan ZHOU was born in 1974 in Wanxian, Sichuan Province. He got his B.S. (1997), M.S. (2000), Ph.D. (2003), postdoctoral fellow (2003–2005), and Associate Professor (2005–) from Nanjing University. He was an Alexander von Humboldt Research Fellow (2006.10–2008.06) in Rostock University (Host professor: Prof. Dr. Christoph Schick). He was an Awardee of the National 100 Excellent Ph.D. Dissertations (2005, Supervisor: Prof. Dr. Gi Xue). His research interests are conformation transition, phase transition, glass transition of polymers, fast scanning and sensitive calorimetry, metastable materials and confinement effect.

References

1. Jones, J. B.; Barenbergt, S.; Geil, P. H., *Polymer* **1979**, *20*, 903
2. Zhang, J. H.; Zhao, Y. S., *Nature* **2004**, *430*, 332
3. Velikov, V.; Borick, S.; Angell, C. A., *Science* **2001**, *294*, 2335
4. Inoue, A., *Prog. Mater Sci*. **1998**, *43*, 365
5. Brucato, V.; Piccarolo, S.; La Carrubba, V., *Chem. Eng. Sci*. **2002**, *57*, 4129
6. Lai, S. L.; Guo, J. Y.; Petrova, V.; Ramanath, G.; Allen, L. H., *Phys. Rev. Lett*. **1996**, *77*, 99
7. Denlinger, D. W.; Abarra, E. N.; Allen, K.; Rooney, P. W.; Messer, M. T.; Watson, S. K.; Hellman, F., *Rev. Sci. Instrum*. **1994**, *65*, 946
8. Efremov, M. Y.; Schiettekatte, F.; Zhang, M.; Olson, E. A.; Kwan, A. T.; Berry, R. S.; Allen, L. H., *Phys. Rev. Lett*. **2000**, *85*, 3560
9. Efremov, M. Y.; Olson, E. A.; Zhang, M.; Zhang, Z.; Allen, L. H., *Phys. Rev. Lett*. **2003**, *91*, 85703
10. Lai, S. L.; Ramanath, G.; Allen, L. H.; Infante, P.; Ma, Z., *Appl. Phys. Lett*. **1995**, *67*, 1229
11. Efremov, Y.; Olson, E. A. Z. M.; Lai, S. L.; Schiettekatte, F.; Zhang, Z. S.; Allen, L. H., *Thermochim. Acta*. **2004**, *412*, 13
12. Efremov, M. Y.; Olson, E. A.; Zhang, M.; Schiettekatte, F.; Zhang, Z.; Allen, L. H., *Rev. Sci. Instrum*. **2004**, *75*, 179
13. Lopeandía, A. F.; Cerdó, L. I.; Clavaguera-Mora, M. T.; Arana, L. R.; Jensen, K. F.; Muñoz, F. J.; Rodríguez-Viejoa, J., *Rev. Sci. Instrum*. **2005**, *76*, 65104
14. Lai, S. L.; Carlsson, J. R. A.; Allen, L. H., *Appl. Phys. Lett*. **1998**, *72*, 1098
15. Efremov, M. Y.; Warren, J. T.; Olson, E. A.; Zhang, M.; Kwan, A. T.; Allen, L. H., *Macromolecules* **2002**, *35*, 1481
16. Efremov, M. Y.; Olson, E. A.; Zhang, M.; Zhang, Z.; Allen, L. H., *Macromolecules* **2004**, *37*, 4607
17. Lopeandia, A. F.; Rodriguez-Viejo, J., *Thermochimica. Acta*. **2007**, *461*, 82
18. Torrens-Serra, J.; Rodriguez-Viejo, J., *Phys. Rev. B* **2007**, *76*, 214111
19. van Herwaarden, A. W., *Thermochim. Acta*. **2005**, *432*, 192
20. Adamovsky, S. A.; Minakov, A. A.; Schick, C., *Thermochim. Acta*. **2003**, *403*, 55
21. Minakov, A. A.; Mordvintsev, D. A.; Schick, C., *Polymer* **2004**, *45*, 3755
22. Minakov, A. A.; Mordvintsev, D. A.; Schick, C., *Faraday Discuss* **2005**, *128*, 261
23. Ray, V. V.; Banthia, A. K.; Schick, C., *Polymer* **2007**, *48*, 2404
24. Minakov, A. A.; van Herwaarden, A. W.; Wien, W.; Wurm, A.; Schick, C., *Thermochimica. Acta*. **2007**, *461*, 96
25. Minakov, A.; Wurm, A.; Schick, C., *Eur. Phys. J. E* **2007**, *23*, 43
26. De Santis, F.; Adamovsky, S.; Titomanlio, G.; Schick, C., *Macromolecules* **2007**, *40*, 9026
27. Gradys, A.; Sajkiewicz, P.; Minakov, A. A.; Adamovsky, S.; Schick, C.; Hashimoto, T.; Saijo, K., *Mater. Sci. Eng. A* **2005**, *413*, 442
28. Silvestre, C.; Cimmino, S..; Duraccio, D.; Schick, C., *Macromol. Rapid Commun*. **2007**, *28*, 875
29. Pyda, M.; Nowak-Pyda, E.; Heeg, J.; Huth, H.; Minakov, A. A.; Di Lorenzo, M. L.; Schick, C.; Wunderlich, B., *J. Polym. Sci., Part B: Polym. Phys*. **2006**, *44*, 1364
30. Tol, R. T.; Minakov, A. A.; Adamovsky, S. A.; Mathot, V. B. F.; Schick, C., *Polymer* **2006**, *47*, 2172
31. Minakov, A. A.; Mordvintsev, D. A.; Tol, R.; Schick, C., *Thermochim. Acta.* **2006**, *442*, 25
32. Minakov, A. A.; Schick, C., *Rev. Sci. Instrum.* **2007**, *78*, 73902
33. Adamovsky, S.; Schick, C., *Thermochim. Acta*. **2004**, *415*, 1
34. Schönhals, A.; Schick, C.; Huth, H.; Frick, B.; Mayorova, M.; Zorn, R., *Polym. Mater. Sci. Eng*. **2007**, *97*, 948
35. Huth, H.; Wang, L. M.; Schick, C.; Richert, R., *J. Chem. Phys*. **2007**, *126*, 104503
36. Huth, H.; Minakov, A. A.; Schick, C., *J. Polym. Sci. B Polym. Phys*. **2006**, *44*, 2996
37. Lupascu, V.; Huth, H.; Schick, C.; Wübbenhorst, M., *Thermochim. Acta*. **2005**, *432*, 222
38. Wahid, S. M. S.; Madhusudana, C. V., *Intern*. J. *Heat. Mass. Transf*. **2003**, *46*, 4139
39. Rao, V. V.; Bapurao, K.; Nagaraju, J.; Krishna Murthy, M. V., *Meas. Sci. Technol*. **2004**, *15*, 275
40. Slifka, A. J.; Filla, B. J.; Phelps, J. M., *J. Res. Natl. Inst. Stand. Technol*. **1998**, *103*, 357
41. Xu, Y.; Luo, X.; Chung, D. D. L., *J. Electr. Packaging* **2002**, *124*, 188
42. Polyanin, A. D., Handbook on Linear Partial Differential Equations for Engineers and Scientists. London, Chapman and Hall/CRC.; 2002
43. Revaz, B.; Zink, B. L.; O'Neil, D.; Hull, L.; Hellman, F., *Rev. Sci. Instr.* **2003**, *74*, 4389
44. Minakov, A.; Morikawa, J.; Hashimoto, T.; Huth, H.; Schick, C., *Meas. Sci. Technol*. **2006**, *17*, 199
45. Minakov, A. A.; Adamovsky, S. A.; Schick, C., *Thermochim. Acta*. **2005**, *432*, 177
46. Minakov, A. A., *Thermochim. Acta*. **1997**, *305*, 165

47. Hatta, I.; Minakov, A. A., *Thermochim. Acta*. **1999**, *330*, 39
48. Minakov, A. A., *Thermochim. Acta*. **2000**, *345*, 3
49. Technical. data available on the website: http, //www.2spi.com/catalog/vac/apiezon-ncryo.html
50. Keller, A.; Cheng, S. Z. D., *Polymer* **1998**, *19*, 4461
51. Reiter, G.; Strobl, G., Progress in Understanding of Polymer Crystallization. Mulhouse. Freiburg, Springer-Verlag, 2006
52. Strobl, G. R., The Physics of Polymers. Berlin, Springer.; 1997.
53. Beekmans, L. G. M.; van der Meer, D. W.; Vancso, G. J., *Polymer* **2002**, *43*, 1887
54. Ivanov, D. A.; Amalou, Z.; Magonov, S. N., *Macromolecules* **2001**, *34*, 8944
55. Beekmans, L. G. M.; Vancso, G. J., *Polymer* **2000**, *41*, 8975
56. Jiang, Y.; Yan, D. D.; Gao, X.; Han, C. C.; Jin, X. G.; Li, L.; Wang, Y.; Chan, C. M., *Macromolecules* **2003**, *36*, 3652
57. Sohn, S.; Alizadeh, A.; Marand, H., *Polymer* **2000**, *41*, 8879
58. Sauer, B. B.; Kampert, W. G.; Blanchard, E. N.; Threefoot, S. A.; Hsiao, B. S., *Polymer* **2000**, *41*, 1099
59. Wang, Z. G.; Hsiao, B. S.; Sauer, B. B.; Kampert, W. G., *Polymer* **1999**, *40*, 4615
60. Xu, H.; Ince, B. S.; Cebe, P., *J. Polym. Sci. B Polym. Phys*. **2003**, *41*, 3026
61. Holdsworth, P. J.; Turner-Jones, A., *Polymer* **1971**, *12*, 195
62. Kampert, W. G.; Sauer, B. B., *Polymer* **2001**, *42*, 8703
63. Kim, H. G.; Robertson, R. E., *J. Polym. Sci. B Polym. Phys*. **1998**, *36*, 133
64. Pijpers, M. F. J.; Mathot, V. B. F.; Goderis, B.; Scherrenberg, R.; van der Vegte, E., *Macromolecules* **2002**, *35*, 3601
65. Hoffman, J. D.; Weeks, J. J., J. *Res. Nat. Bur. Stand. Sect. A* **1962**, *66A*, 13
66. Yamada, K.; Hikosaka, M.; Toda, A.; Yamazaki, S.; Tagashira, K., *Macromolecules* **2003**, *36*, 4790
67. Yamada, K.; Hikosaka, M.; Toda, A.; Yamazaki, S.; Tagashira, K., *Macromolecules* **2003**, *36*, 4802
68. Belonoshko, A. B.; Skorodumova, N. V.; Rosengren, A.; Johansson, B., *Phys. Rev. B* **2006**, *73*, 12201
69. Bai, X. M.; Li, M., *Phys. Rev*. **2005**, *72*, 52108.
70. Fecht, H. J.; Johnson, W. L., *Nature* **1988**, *334*, 50
71. Tallon, J. L., *Nature* **1989**, *342*, 658
72. Lindemann, F. A., *Z. Phys*. **1910**, *11*, 609
73. Born, M., *J. Chem. Phys*. **1939**, *7*, 591
74. Lu, K.; Li, Y., *Phys. Rev. Lett*. **1998**, *80*, 4474
75. Strobl, G., *Prog. Polym. Sci*. **2006**, *31*, 398
76. Wunderlich, B., *Thermochim. Acta*. **2005**, *432*, 148
77. Wunderlich, B., *Thermochim. Acta*. **2005**, *432*, 127
78. Wunderlich, B., *Thermochim. Acta*. **2003**, *403*, 1
79. Hellmuth, E.; Wunderlich, B., *J. Appl. Phys*. **1965**, *36*, 3039
80. Clements, J.; Ward, I. M., *Polymer* **1982**, *23*, 935
81. Schawe, J. E. K.; Strobl, G. R., *Polymer* **1998**, *39*, 3745
82. Toda, A.; Hikosaka, M.; Yamada, K., *Polymer* **2002**, *43*, 1667
83. Cebe, P., *J. Polym. Sci. B Polym. Phys*. **2005**, 43, 629
84. Merzlyakov, M., *Thermochim. Acta*. **2003**, *403*, 65
85. Sullivan, P. F.; Seidel, G., *Phys. Rev*. **1968**, *173*, 679
86. Yao, H.; Ema, K.; Hatta, I., *Jpn. J. Appl. Phys. Part 1* **1999**, *38*, 945
87. Donth, E., Glass Transition. Berlin, Springer, **2001**
88. Hensel, A. S. C., *J. Non-Cryst. Solids* **1998**, *235*, 510
89. Minakov, A. A.; Roy, S. B.; Bugoslavsky, Y. V.; Cohen, L. F., *Rev. Sci. Instrum*. **2005**, *76*, 43906
90. Schonhals, A.; Schick, C.; Huth, H.; Frick, B.; Mayorova, M.; Zorn, R., *J. Non-Cryst. Solids* **2007**, *353*, 3853
91. Schönhals, A.; Goering, H.; Schick, C.; Frick, B.; Mayorova, M.; Zorn, R., *Eur. Phys. J. Special Topics* **2007**, *141*, 255
92. Schönhals, A.; Goering, H.; Schick, C., *Mater. Res. Soc. Symp. Proc. E* **2005**, *899*, 0501
93. Huth, H.; Minakov, A.; Schick, C., *Netsu. Sokutei*. **2005**, *32*, 70
94. Brás, A. R.; Dionísio, M.; Huth, H.; Schick, C.; Schönhals, A., *Phys. Rev. E* **2007**, *75*, 61708
95. Weyer, S.; Hensel, A.; Schick, C., *Thermochim. Acta*. **1997**, *305*, 267
96. Williams, M. L.; Landel, R. F.; Ferry, D. J., *J. Am. Chem. Soc*. **1955**, *77*, 3701
97. Huth, H.; Minakov, A. A.; Serghei, A.; Kremer, F.; Schick, C., *Eur. Phys. J. Special Topics* **2007**, *141*, 153
98. Keddie, J. L.; Jones, R. A. L.; Cory, R. A., *Europhys. Lett*. **1994**, *27*, 59
99. Fakhraai, Z.; Forrest, J. A., *Phys. Rev. Lett*. **2005**, *95*, 25701
100. Wunderlich, B., *Pure Appl. Chem*. **1995**, *67*, 1019